Chapter 6
Materials for Micro Forming

Hans-Werner Zoch, Alwin Schulz, Chengsong Cui, Andreas Mehner, Julien Kovac, Anastasiya Toenjes and Axel von Hehl

H.-W. Zoch (✉) · A. Schulz (✉) · C. Cui · A. Mehner (✉) · J. Kovac · A. Toenjes (✉) · A. von Hehl
Leibniz Institute for Materials Engineering—IWT, University of Bremen, Bremen, Germany
e-mail: zoch@iwt-bremen.de

A. Schulz
e-mail: aschulz@iwt-bremen.de

A. Mehner
e-mail: mehner@iwt-bremen.de

A. Toenjes
e-mail: toenjes@iwt-bremen.de

6.1 Introduction to Materials for Micro Forming

Hans-Werner Zoch

Thin metallic foils with a thickness below 50 μm are required for deep drawing of sub millimeter micro components. Commercial metallic foils for deep drawing are typically made of highly ductile materials such as pure aluminum, copper or stainless steel. Yet these materials are not suited for deep drawing of high strength micro components. Alloys with high mechanical strength are not available as thin foils below 50 μm due to significant strain hardening during the cold rolling process. Therefore, an alternative process based on physical vapor deposition (PVD) was developed, in order to produce thin metallic foils with improved mechanical properties. Thin foils of high strength aluminum alloys containing scandium and zirconium (Al–Sc–Zr), heat treatable martensitic chromium steels (X70Cr13) and high manganese austenitic steels (X5MnSiAl25-3-3) were produced by PVD magnetron sputtering onto thin substrate foils which were removed by selective etching after the PVD deposition process. Microstructure, mechanical properties and the effect of post annealing of these monometallic PVD foils were studied in order to find optimized processing parameters for deep drawing of micro components with advanced mechanical properties. Additionally, bimetallic PVD foils were produced and successfully tested for deep drawing of high strength micro components. Also, a prototype device for continuous physical vapor deposition onto thin metallic substrate tapes for an industrial scalable production of thin bimetallic PVD foils was developed, built and successfully tested.

Heat treatment processes within the manufacturing chain of micro components, either have the target to restore ductility or deformability after a cold rolling or deep drawing process, or are used to increase the final strength of the finished component. For single piece production and high volume production as well, short-term heat treatment processes have advantages compared to long-term heat treatments.

Because of the very small dimensions of the micro components and their distortion sensitivity, a new furnace design was developed—the drop-down tube furnace. Parts falling through an indirect heated tube of 6 m height are heated by radiation during falling down. As there is no mechanical contact, no distortion or damage of the parts occurs. Surface reactions are prevented by protective gas, e.g. when components see a short recrystallization annealing to recover deformability after cold working. Cooling in air or nitrogen gas at the furnace outlet allows to martensitic harden heat treatable steels. In the case of precipitation hardening of aluminum alloys, the heating times are too short for solution annealing, yet aging treatments during falling down of still supersaturated alloys as created by PVD sputtering processes are possible to increase strength.

In forming processes for micro components specific properties are required for the raw materials. If the principal dimensions of the workpiece and the corresponding tool are reduced to the micro scale these requirements are even more pronounced. Especially for the tools the microstructural phase distribution should

be fine and very homogenous. When hard carbides are necessary for wear resistance powder metallurgical methods are suitable to achieve the desired properties. Among those technologies spray forming has the capability to produce free-standing near net shape products from the melt. The combination of two spray-forming assemblies, the so called co-spray forming, gives the opportunity to produce bulk materials with different local chemical compositions and a gradient in between. This allows the design of tools with different properties in specific areas. Using tool steels gives additional possibilities by adjusting hardness via specific heat treatments. In this chapter co-spray forming is shown to produce graded high-alloyed tool steels. The challenge of simultaneously hardening of different microstructures is solved by induction heat treatment, finally leading to materials that could be hard machined to swaging tools. These tools have been used for micro swaging of wires from austenitic stainless steels.

6.2   Tailored Graded Tool Materials for Micro Cold Forming via Spray Forming

Alwin Schulz[*] **and Chengsong Cui**

Abstract In micro cold forming, the tools are loaded differently in various functional areas, and tailored material properties are therefore required. To meet this requirement, different tool steels can be applied in the specific regions of the tools, with a gradual material transition in between to ensure a good bonding. These kinds of composite material can be produced via two newly developed material manufacturing processes: co-spray forming and successive spray forming. The spray-formed materials have been hot formed to eliminate porosity and break up the carbide network. Moreover, a selective heat treatment based on middle frequency induction heating has been developed to simultaneously austenitize the tool steels at different temperatures since the different steels may require different heat treatment conditions. Finally, micro rotary swaging tools made of graded tool steels have been precisely machined in hardened condition due to the fine and homogeneous microstructure in the steels. The tools have been successfully applied to form wires of AISI 304 stainless steel.

Keywords Manufacturing process · Tool steel · Spray forming

6.2.1   Introduction

In cold forming of micro metallic components, the loads on the forming tools vary in different functional regions, so tailored material properties in the specific regions are required. For example, the reduction zone of an infeed rotary swaging tool should be hard and wear-resistant to ensure high compact pressure and high friction, while the calibration zone of the tool should be strong but also micro-machinable, since the radius of the calibration zone is smaller than 1 mm. To meet these requirements, different tool steels may be applied in the specific regions of the tools. A gradual material transition in between is expected to reduce critical stresses at the interface and ensure good bonding of the different materials.

Components adapted to the specific loads in different areas by material modification or sequential construction have long been manufactured by means of plating, cladding, thermal spraying, electroplating, PVD and CVD. These methods have in common that a relatively sharp transition between the base material and functional layer is formed. The chemical bonding at the interfaces is weakened due to different crystal structures and lattice parameters [Wan96]. Process-related residual stresses at the interfaces further limit the loading capacity of the composites [Sun01]. In addition, different thermal expansions of the base material and the functional layer at elevated temperatures, e.g. as a result of unlubricated frictional

contact, lead to additional thermal stresses [Kho00]. These limitations are coun-teracted by an intermediate layer between the functional layer and the base material, which serves to mediate differences in the crystal structure, lattice parameters and thermal stresses [Mus92]. If the functional layer is formed by the reaction of several components, as in the case of TiN layer via PVD or CVD, gradients can be built up within a layer. Graded layer structures can also be generated during thermal spraying by mixing different powders in the flame [Mus92]. These gradients are metal–matrix composites (NiCr–ZrO$_2$) with different mixing ratios, but the grading is limited by the particle size, since the fine powders are difficult to process [Peu05]. Moreover, the thermal cycles during thermal spraying are so short that homogen-ization of the material is hard to achieve by mixing of the melts or by diffusion over longer distances [Söl92].

Spray forming is an advanced material manufacturing process, in which a stream of alloy melt is atomized and the resultant small droplets are spray-deposited on a moving substrate, resulting in a near-net-shaped product with fine and homogen-eous microstructure [Hen17]. As a new development of the process, two different alloys are melted simultaneously, and broken up into droplets in two spray cones via two free-fall atomizers, resulting in two-layered flat deposits as shown in Fig. 6.1a [Mey09]. If the two spray cones partially overlap, a gradient zone is generated in the two-layered flat deposits [Cui13]. An alternative spray forming process to produce graded materials is to spray two different alloys into a ring-shaped deposit (see Fig. 6.1b) [Cui16]. A gradual material transition can also be generated in the deposit if the two melts are mixed incrementally in the tundish. These two spray forming processes, which overcome the problems encountered by the conventional processes mentioned above, are expected to result in graded tool
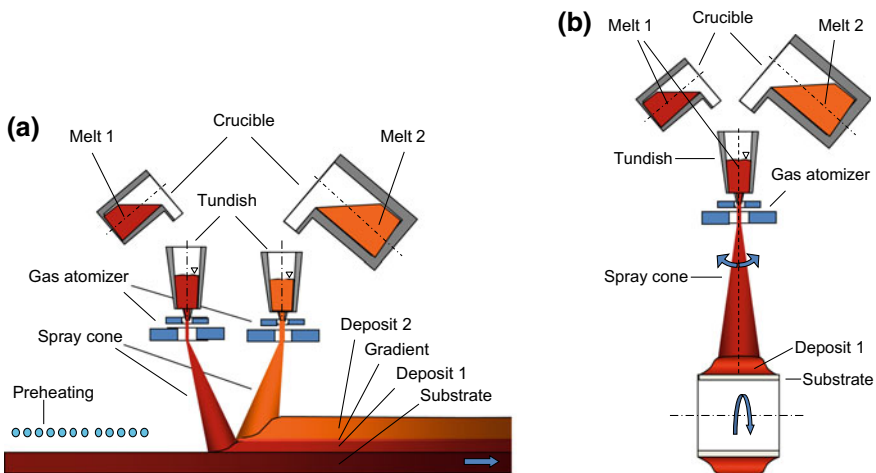

Fig. 6.1 Schematic drawings of **a** co-spray forming of a flat graded deposit, and **b** successive spray forming of a ring-shaped graded deposit [Cui16]

materials that meet the requirements of micro cold forming. In the following section, these two spray forming processes will be introduced, and the spray-formed graded tool materials will be characterized and evaluated.

Moreover, a selective heat treatment based on middle frequency induction heating and inductor oscillation has been developed and tested to simultaneously austenitize the tool steels at different temperatures since the different steels may require different heat treatment conditions to achieve optimal material properties.

Finally, the machinability of the graded tool materials will be assessed and the performance of the graded tools in micro cold forming will be demonstrated.

6.2.2 Production of Graded Tool Materials

6.2.2.1 Materials Selection

Three tool steels have been selected for the spray forming of graded tool materials for micro cold forming. The nominal chemical composition of the steels is listed in Table 6.1. The large amount of vanadium-rich carbides in the high-speed steel HS6-5-3C is responsible for its high hardness and excellent wear resistance. The HS6-5-2C is similar to the HS6-5-3C, and it shows relatively higher fracture toughness due to lower contents of V and C and hence a smaller amount of carbides. Compared with the high-speed steels, the cold work tool steel X110CrMoV8-2 has an even lower content of hard carbides and significantly higher fracture toughness, which leads to better micro-machinability and fracture toughness. In this study, two material combinations for the graded tool materials have been investigated: HS6-5-3C/HS6-5-2C, and HS6-5-3C/X110CrMoV12.

6.2.2.2 Spray Forming of Graded Tool Materials

Spray forming of graded tool materials is illustrated in Figs. 6.1 and 6.2: co-spray forming of flat deposits [Cui13], and successive spray forming of ring-shaped deposits [Cui16].

During the former process two tool steels are melted and gas-atomized separately and co-spray-deposited on a translating flat substrate, resulting in a flat

Table 6.1 Nominal chemical composition of tool steels

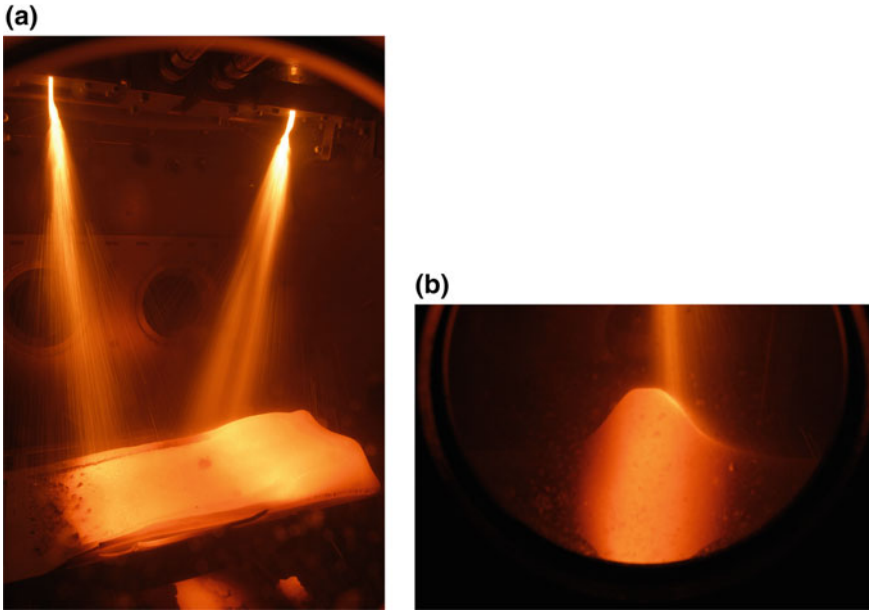| Steel grade		Chemical element, wt%				
Description	AISI type	C	Cr	W	Mo	V
HS6-5-3C	M3:2	1.3	4.2	6.3	5.0	3.0
HS6-5-2C	M2	0.9	4.0	6.4	5.0	1.9
X110CrMoV8-2	–	1.0	8.0	–	2.5	0.3

Fig. 6.2 Photographs of **a** co-spray forming of a flat graded deposit, and **b** successive spray forming of a ring-shaped graded deposit

composite deposit with a gradual transition of the chemical composition in between when the two spray cones partially overlap [Cui13a]. By this method, different microstructure and mechanical properties can be combined in a single deposit. In addition, fine and homogeneous microstructure can be achieved in the spray-formed materials due to rapid solidification and droplet fragmentation during the spray forming process.

During the latter process two different tool steels are also melted separately in two crucibles. One melt is poured first into a tundish, followed by gas atomization and spray deposition on a rotating tubular substrate, resulting in a ring-shaped deposit (inner ring). When the first crucible is empty, the second steel melt is poured into the same tundish, gas-atomized and spray-deposited on top of the inner ring to form an outer ring. If there is still a quantity of the first melt in the tundish when the second melt is poured into it, they mix in the tundish and the proportion of the second steel increases gradually as it is continuously added. Consequently, a gradient is also generated inside the deposit, depending on the gradational mixture of the two melts in the tundish. In comparison with the co-spray forming process, the successive spray forming process is more suitable for the manufacture of thick deposits since less heat is accumulated in the deposit during spray forming due to rotation of the deposit, and therefore lower thermal stresses and lower distortion are generated in the deposit.

Co-spray forming of the graded tool steels was carried out in the facility SK1+ at the University of Bremen. Firstly, flat deposits of HS6-5-3C/HS6-5-2C and HS6-5-3C/X110CrMoV8-2 with a thickness of approx. 30 mm were spray-formed (Fig. 6.3a). The tilting angles of the spray cones were varied at 6°, 9° and 12° to achieve different thicknesses of the gradient zone. In addition, the atomization gas pressure was adjusted to achieve different thermal conditions, which influence the porosity and the microstructure of the deposits. Secondly, flat deposits with a thickness of 55–60 mm (Fig. 6.3b) were produced by reducing the translational speed of the substrate; therefore, after hot deformation, the graded materials are still thick enough for making micro forming tools. In order to provide thicker semi-finished materials for fabricating the micro forming tools and to further increase the degree of deformation of the deposits, the co-spray forming process was modified to produce flat graded deposits with a thickness of about 100 mm (Fig. 6.3c). This modified spray forming process consisted of two phases. In the first phase, co-spray forming was conducted, similar to that for the deposits with a thickness of 55–60 mm. In the second phase, the substrate moved backward when the melt for the lower layer of the deposit was ended, and the melt for the upper layer of the deposit was continuously sprayed over the graded deposit. Consequently, thicker deposits were produced.

Successive spray forming of graded tool steels was also carried out in the facility SK1+ [Cui16]. During this process, the tool steels (HS6-5-3C and X110CrMoV8-2) were melted separately and spray-deposited successively on a rotating tubular substrate, resulting in a ring-shaped graded deposit with an outer diameter of about 335 mm and an inner diameter of 114 mm.

To reduce the hardness and remove stresses, the spray-formed deposits were soft annealed by heating to 840 °C at the rate of 50 K/h, holding for 4 h, followed by cooling to 500 °C at the rate of 20 K/h and uncontrolled cooling in the furnace to room temperature.

6.2.2.3 Densification of Graded Tool Materials

Porosity is an unavoidable characteristic of spray-formed materials [Hen17]. Four approaches have been applied for the densification of the spray-formed graded tool steels:
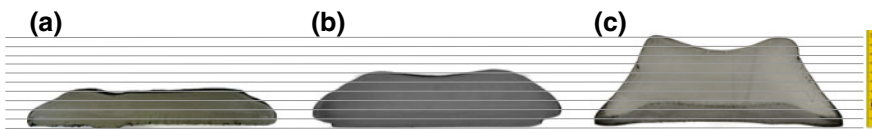

Fig. 6.3 Transverse sections of flat deposits of different thickness around **a** 30 mm, **b** 60 mm, and **c** 100 mm

(1) Samples from the 30 mm thick flat deposits were HIPped at 1140 °C under the pressure of 100 MPa for 3 h. Generally, the porosity is eliminated by HIPping. However, for deposits with open porosity, the HIPping should be conducted in capsule. It was also found that the carbide networks in the spray-formed deposits remained unchanged after HIPping, which would impair the fracture toughness of the materials.

(2) Samples from the 30 mm thick flat deposits were hot rolled on a lab rolling mill to eliminate porosity and break up the carbide network [Cui14]. The samples (thickness 24–28 mm after milling) were preheated in a furnace to 1100 °C, held at that temperature for 10–30 min, and rolled in three passes to a final thickness of approximately 10 mm. For each rolling pass, the true strain and the true strain rate of the rolled samples were in the range of 0.2–0.4 and 2–3 s^{-1}, respectively. The total strain of the samples was about 0.9. Samples from the 60 mm thick flat deposits were also hot rolled on this lab rolling mill. The samples (thickness 44–49 mm after milling) were preheated to 1100 °C and rolled in three passes to a final thickness of approximately 24 mm. For each rolling pass, the true strain and true strain rate of the sample were 0.2–0.3 and 1–2 s^{-1}, respectively. The total strain of the sample was around 0.7.

(3) The 100 mm thick flat deposits were hot forged to eliminate porosity and break up the carbide network. The deposits were forged in a temperature range from 1150 °C to 950 °C to a thickness of approximately 50 mm and cooled slowly in dry sand.

(4) The spray-formed ring-shaped deposit was machined to a ring preform (318 mm OD × 125 mm ID × 50 mm), and forwarded to a rolling mill for direct ring production. The deposit was preheated in a furnace to 1100 °C and rolled to the final dimensions (543 mm OD × 431 mm ID × 39 mm). The area reduction of the ring was 2.23. After ring rolling, the sample was cooled slowly in the furnace from 860 °C to room temperature.

6.2.2.4 Heat Treatment

The different materials in the graded deposits usually require different heat treatment conditions. For example, the recommended austenitization temperatures for high-speed steels are much higher than those for cold work tool steels. If the graded deposits are austenitized at high temperatures, too much austenite may be retained in the cold work tool steels and the grain structure would be coarsened. If the graded deposits are austenitized at low temperatures, insufficient dissolution of carbides may hinder the secondary hardening of the high-speed steels. Due to that, for the graded deposits made of different steels, any compromise for heat-treating in a furnace should lead to insufficient hardening results.

To demonstrate this, samples of the graded deposits were austenitized in a vacuum furnace at 1080 °C for 20 min or at 1180 °C for 10 min, and quenched with nitrogen at 0.6 MPa, followed by triple tempering at 550 °C for 2 h. It was

found that the austenitization temperature of 1180 °C was suitable for the HS6-5-3C and HS6–5-2C, but too high for the X110CrMoV8-2 (see Fig. 6.11). The appropriate austenitization temperature for X110CrMoV8-2 must not exceed 1080 °C. Therefore, the traditional austenitization in a furnace is not suitable for hardening of graded materials like HS6-5-3C/X110CrMoV8-2.

To overcome this problem, a selective heat treatment based on induction heating with an oscillating inductor has been developed, as shown in Fig. 6.4. An oscillating ring-shaped inductor is used to heat the cylindrical sample. The upper region of the sample is HS6-5-3C and the lower region is X110CrMoV8-2. Between the two alloys is the gradient zone. The desired austenitization temperatures for HS6-5-3C and X110CrMoV8-2 are T1 and T2, respectively. Middle frequency induction is applied for a thorough heating from the surface to the core of the sample. The induction heating process is divided into three phases:

Phase 1: The complete sample is heated up to the temperature T2 (desired for X110CrMoV8-2) by oscillating the inductor over the complete sample.

Phase 2: The inductor continues to oscillate over the complete sample but the inductor current is reduced, so that the sample temperature is held at T2.

Phase 3: The inductor oscillates over the upper region (HS6-5-3C) and the local temperature is further increased to T1 (desired for HS6-5-3C). In order to
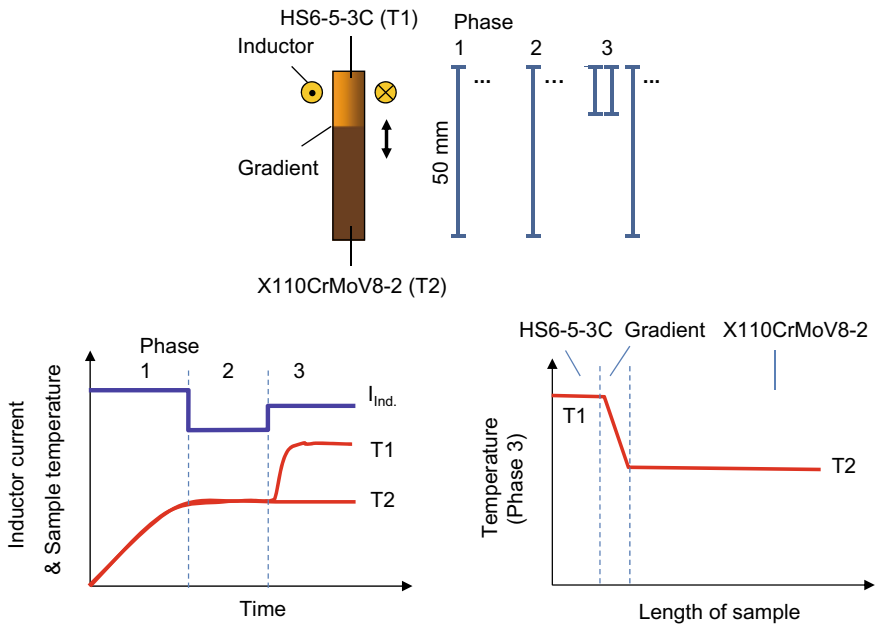

Fig. 6.4 Schematic of the selective heat treatment of a cylindrical sample of the graded material HS6-5-3C/X110CrMoV8-2 based on middle frequency induction heating and oscillation of the inductor [Cui17a] Copyright 2017 by MS&T17. Used with permission

hold the temperature of the lower region at T2, the inductor must also oscillate over the complete sample after several oscillations over the upper region. This combined oscillation is repeated and a tailored austenitization of the composite material is achieved.

In this study, cylindrical samples (∅20 mm × 50 mm) were machined along the thickness of the hot rolled ring for the selective heat treatment. The HS6-5-3C region was approximately 10 mm long, the gradient zone 10 mm, and the X110CrMoV8-2 region 30 mm. For temperature measurement, initial tests were done with samples with ∅1.1 mm holes of different depths for placing sheath thermocouples (∅1 mm, type K).

The induction heat treatment facility used in this study was a VL1000 SINAC 200/300 S MFC from EFD Induction GmbH (see Fig. 6.5). The inductor was a water-cooled single turn copper coil with an inner diameter of 22 mm, a cross-section of 6×6 mm^2, and a wall thickness of 1 mm. Thermal insulation (glass fiber) was applied at both ends of the sample to reduce heat loss. In all experiments, an infrared pyrometer (KTR 1075 from Maurer) and a 2-color (ratio) pyrometer in combination with a video camera with a short wavelength infrared filter (ISR 6-TI Advanced, LumaSense) were used to measure the surface temperature of the sample during the heat treatment.
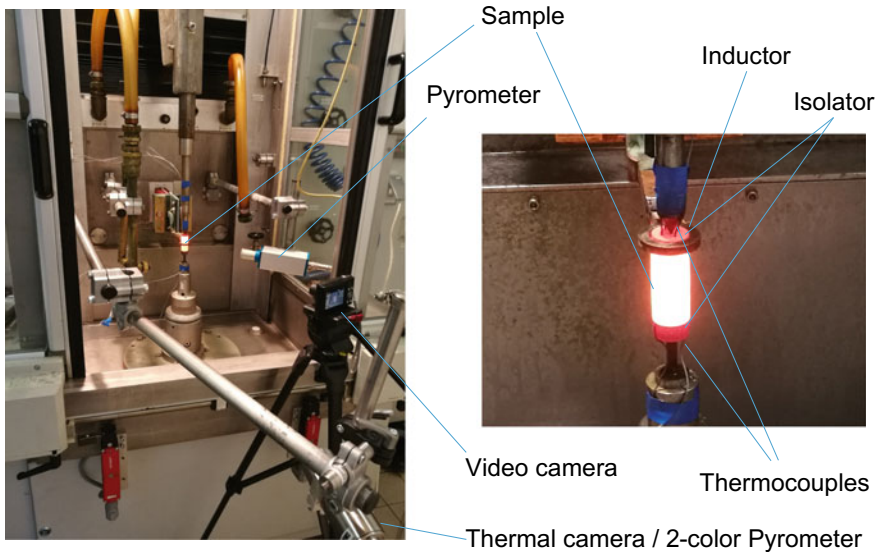

Fig. 6.5 Setup of the selective heat treatment of a cylindrical sample of the graded material HS6-5-3C/X110CrMoV8-2 based on middle frequency (14 kHz) induction heating and oscillation of the inductor

After induction heating, the samples were cooled in air since the tool steels are air hardenable. Finally, the composite samples were tempered three times in a protective atmosphere at 550 °C for 2 h.

The influence of the inductive process parameters (inductor current, motion of inductor, etc.) on the temperature distribution and the result of hardening of the graded materials have been investigated. The microstructure and hardness of the graded materials have been correlated with the austenitizing conditions. More details of the experiments can be found in [Cui17a].

6.2.3 Evaluation of the Graded Tool Materials

6.2.3.1 Co-spray-Formed Material

The distributions of the chemical elements in the co-spray-formed graded materials are most clearly represented by the element vanadium. The measured contents of vanadium over the deposit thickness are given in Fig. 6.6. For both material combinations, the concentration profiles are similar. The effect of the tilting angle of the atomizers on the gradient zone is significant. Tilting the atomizers leads to overlapping of the spray cones and a mixing of the droplets of the two different steels.

Representative microstructure of the graded deposits after hardening and tempering is presented in Figs. 6.7 and 6.8 [Cui13]. The micrographs exhibit equiaxed grain structures with fine carbides, as well as a carbide network at the primary austenite grain boundaries. For both material combinations, there are more MC type carbides in the HS6-5-3C than in the HS6-5-2C or X110CrMoV8-2. The gradient zone shows some intermediate microstructure.

Porosity and carbide networks, which impair the fracture toughness of the materials, have been frequently observed in the spray-formed tool steels. After hot
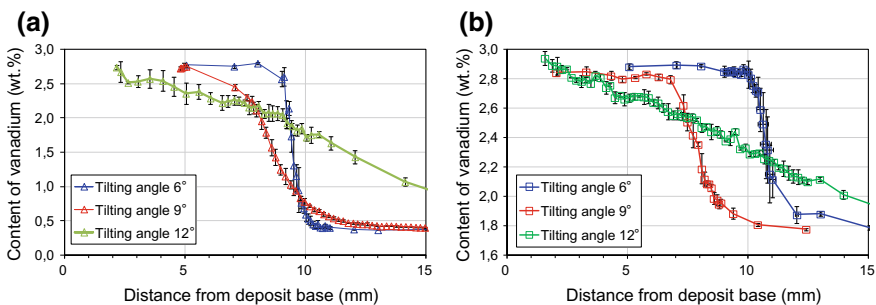

Fig. 6.6 Distribution of the element vanadium in the spray-formed graded deposits of 30 mm thickness depending on the tilting angles of the spray cones: **a** HS6-5-3C/110CrMoV8-2, and **b** HS6-5-3C/HS6-5-2C [Cui13]
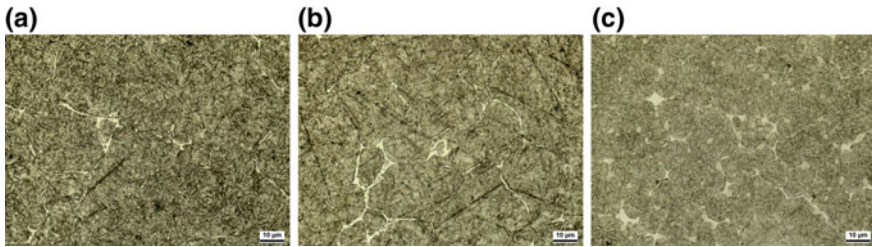
Fig. 6.7 Microstructure of a graded deposit of 30 mm thickness, hardened at 1080 °C and triple tempered at 550 °C: **a** X110CrMoV8-2, **b** X110CrMoV8-2+HS6-5-3C, **c** HS6-5-3C [Cui13]
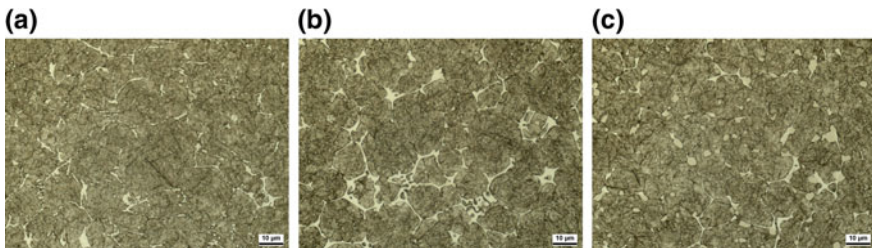

Fig. 6.8 Microstructure of a graded deposit of 30 mm thickness, hardened at 1180 °C and triple tempered at 550 °C: **a** HS6-5-2C, **b** HS6-5-2C+HS6-5-3C, **c** HS6-5-3C [Cui13]

deformation, the porosity has been essentially eliminated, and the coarse carbides have been broken into small pieces. During hot deformation the grain structure might experience a dynamic recrystallization, too. This also resulted in a fine and homogeneous microstructure, as shown in Figs. 6.9 and 6.10.

The hardness values of the graded deposits after hardening as well as after hardening plus tempering are shown in Fig. 6.11:
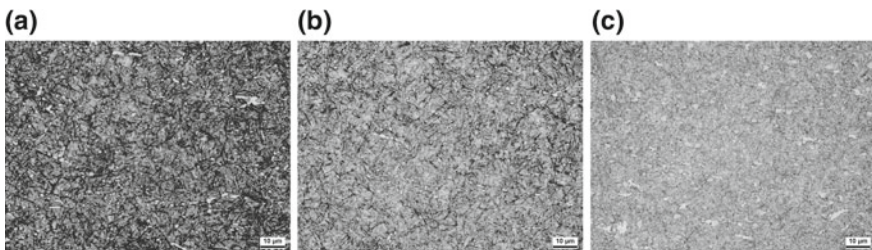

Fig. 6.9 Microstructure of a graded deposit of 30 mm thickness, hot rolled to 10 mm, hardened at 1080 °C and triple tempered at 550 °C: **a** X110CrMoV8-2, **b** X110CrMoV8-2+HS6-5-3C, **c** HS6-5-3C
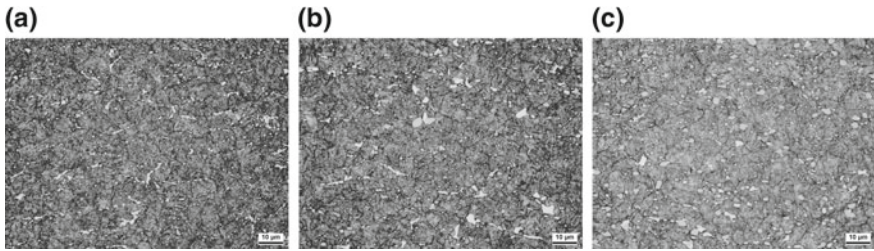
Fig. 6.10 Microstructure of a graded deposit of 30 mm thickness, hot rolled to 10 mm, hardened at 1180 °C and triple tempered at 550 °C: **a** HS6-5-2C, **b** HS6-5-2C+HS6-5-3C, **c** HS6-5-3C
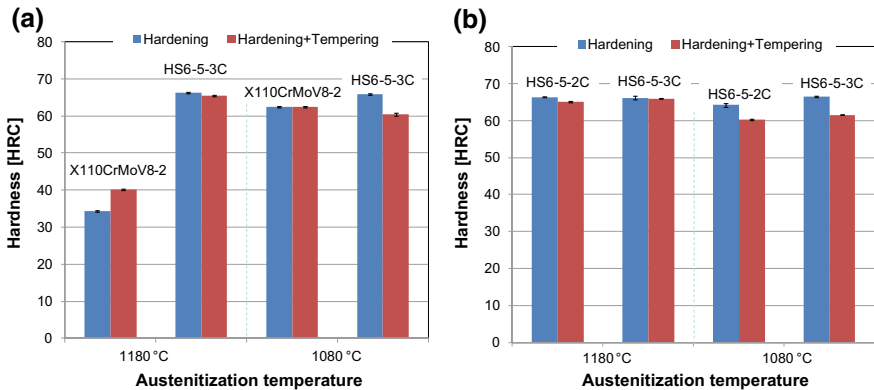

Fig. 6.11 Hardness of graded deposits after hardening and tempering: **a** X110CrMoV8-2/HS6-5-3C, and **b** HS6-5-2C/HS6-5-3C [Cui13]

(1) The hardness of the as-hardened X110CrMoV8-2 with the austenitization temperature of 1180 °C is very low (around 34 HRC). Its hardness increases to 62 HRC with the austenitization temperature of 1080 °C. This indicates that carbide dissolution in the matrix of X110CrMoV8-2 is too high during austenitization at 1180 °C. It results in a very low martensitic transformation temperature and therefore too much retained austenite after quenching. The hardness of the as-hardened HS6-5-3C with the austenitization temperature of 1180 °C is about 66 HRC. It is nearly the same for the austenitization temperature of 1080 °C due to the high carbon content and high alloying element content of this steel. After three times of tempering at 550 °C, the hardness of the X110CrMoV8-2 austenitized at 1180 °C increases to 40 HRC, indicating further transformation of retained austenite. For the X110CrMoV8-2 austenitized at 1080 °C, its hardness remains nearly the same after tempering. For the HS6-5-3C austenitized at 1180 °C, its hardness decreases slightly after tempering. However, for the HS6-5-3C austenitized at 1080 °C, its hardness decreases significantly to about 61 HRC. The relatively low austenitization
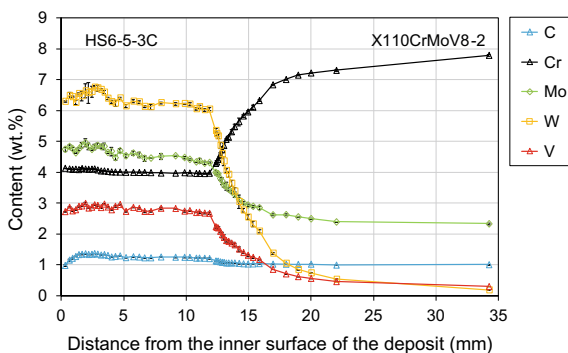
temperature leads to a higher degree of softening during tempering of the high-alloyed steel, and this could not be compensated by secondary hardening because fewer carbides were dissolved during austenitization. It is therefore concluded that a tailored austenitization for this material combination is needed to achieve the optimal material properties for both steels.

(2) For the graded steels HS6-5-3C/HS6-5-2C, the hardness of both steels is higher than 60 HRC in the hardened condition as well as in the tempered condition. When austenitized at 1180 °C, the hardness of both the as-hardened steels is around 66 HRC. After tempering, it is about 65–66 HRC because secondary hardening occurs. When austenitized at 1080 °C, the hardness values of the as-hardened HS6-5-2C and HS6-5-3C are about 62 HRC and 66 HRC, respectively. Fewer carbides dissolve in the austenite matrix at this temperature, and particularly the highly stable carbides like tungsten and molybdenum carbides do not dissolve. After tempering, their hardness reduces to approximately 60 HRC due to decomposition of martensite and less secondary hardening. To achieve high hardness, the austenitization temperature of 1180 °C is preferred for this material combination.

6.2.3.2 Successive Spray-Formed Material

The distributions of the main alloying elements C, Cr, Mo, W and V in a ring-shaped graded material (HS6-5-3C/X110CrMoV12) via successive spray forming and ring rolling are presented in Fig. 6.12. The gradient zone between the inner HS6-5-3C and the outer X110CrMoV8-2 is approximately 10 mm thick, starting at the position about 12 mm from the inner surface of the ring. The slope of the gradient of the elements depends on the level of mixture of the two steel melts in the tundish. If there is less melt of the first steel in the tundish when the second steel melt is added, or the second melt is added more quickly, the gradient zone in the spray-formed ring would be narrower.

Fig. 6.12 Distributions of main chemical elements in the as-rolled ring-shaped graded deposit HS6-5-3C/X110CrMoV12 [Cui16]

The microstructure of the graded materials after the selective induction hardening and tempering, as described before, is presented in Fig. 6.13 [Cui17a]. The MC-type carbides were precipitated in the HS6-5-3C region, and mainly eutectic carbides were observed in the X110CrMoV8-2 region. In the gradient zone, a mixed structure of the two steels was constituted. With high austenitization temperatures (1220 °C/1120 °C), the X110CrMoV8-2 region showed coarse martensite and a large amount of retained austenite, while the gradient zone showed very coarse austenite grains and very little martensite. The microstructure of the graded materials austenitized at 1180 °C/1080 °C and 1150 °C/1050 °C looked similar, except that the microstructure in the gradient zone was somewhat coarser under the austenitization condition at 1180 °C/1080 °C. It was hard to find retained austenite in the graded materials processed under these conditions.

The hardness profiles of the graded materials processed under various induction heating conditions are shown in Fig. 6.14. The maximum austenitization temperatures reached in the various regions of the samples are also plotted in the diagrams. It can be summarized as follows:

(1) Graded temperatures are achieved in all the samples. The relatively broad temperature gradients are caused by the heat conduction from the high temperature region to the low temperature region. To reduce the temperature gradient, the heating time for the samples should be shortened.
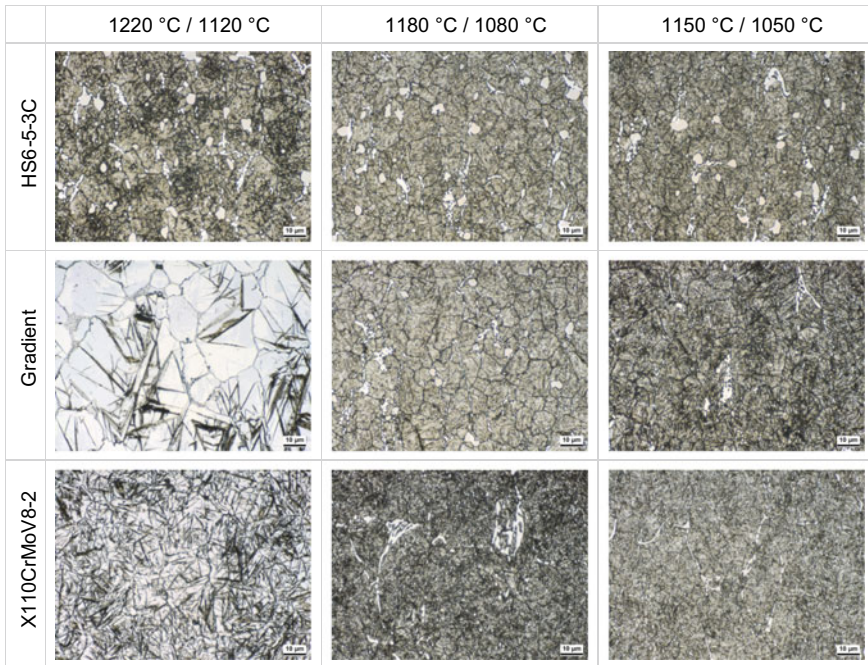

Fig. 6.13 Microstructure of the graded tool steels after selective induction hardening and tempering [Cui17a] Copyright 2017 by MS&T17. Used with permission
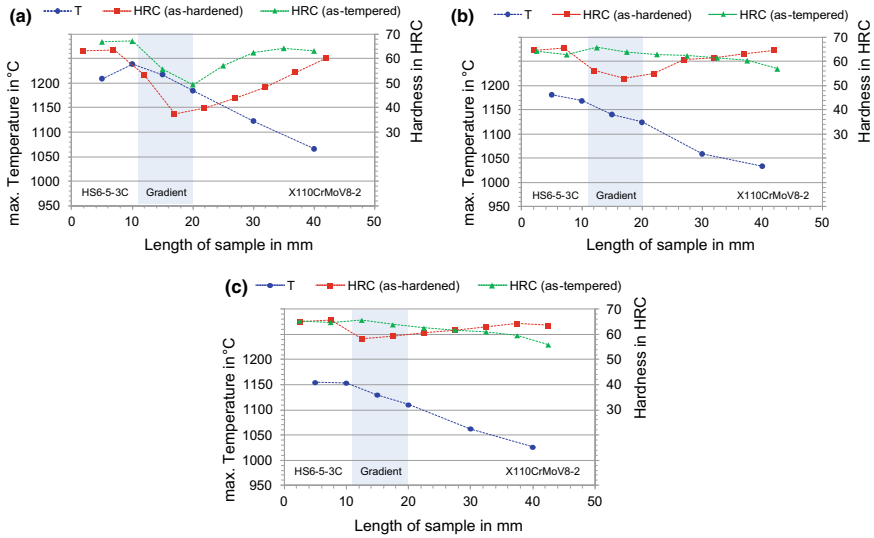
Fig. 6.14 Hardness and maximum austenitization temperature of the graded tool steels processed under various induction heating conditions (target temperatures): **a** 1220 °C/1120 °C, **b** 1180 °C/ 1080 °C, and **c** 1150 °C/1050 °C [Cui17a] Copyright 2017 by MS&T17. Used with permission

(2) The hardness of the gradient zone in the as-hardened condition is low. It increases as the maximum austenitization temperature decreases due to reduced retained austenite. If the austenitization temperature is too high, for example above 1150 °C, excessive dissolution of carbides in the matrix lowers the martensite transformation temperature and results in excessive retained austenite.

(3) The hardness of the gradient zone increases after triple tempering at 550 °C. This is due to the precipitation of fine carbides and further transformation of retained austenite to martensite during the tempering at high temperature. However, if the austenitization temperature is too high, carbide precipitation and further transformation of retained austenite to martensite would be insufficient due to stabilization of the austenite, resulting in a soft gradient zone (see Fig. 6.14a).

(4) In Fig. 6.14b the maximum austenitization temperature is approximately 1180 °C in the HS6-5-3C region and 1060 °C in the X110CrMoV8-2 region. After induction hardening the hardness of the HS6-5-3C steel and the X110CrMoV8-2 steel can reach 65 HRC, while the hardness of the gradient zone is low (52 HRC at the length position 17 mm). After tempering, the hardness of the gradient zone increases to 62–65 HRC. At lower austenitization temperatures (target temperatures: 1150 °C/1050 °C), the hardness of the gradient zone is further increased (Fig. 6.14c). After tempering, the hardness profiles are similar to that shown in Fig. 6.14b.

(5) If the austenitization temperature for X110CrMoV8-2 is very low (for example below 1050 °C), secondary hardening is insufficient and its hardness decreases after tempering (position around 40 mm in Fig. 6.14b, c). A high austenitization temperature is preferred for HS6-5-3C since it contributes to carbide dissolution and secondary hardening.

6.2.4 Fabrication of Micro Cold Forming Tools

Micro forming tools have been fabricated from the co-spray-formed graded steels. For plunge rotary swaging tools the tool surface consisted of HS6-5-3C (hard and wear-resistant), the tool body of X110CrMoV8-2 or HS6-5-2C (fracture-resistant and tough), with the gradient zone in between. For infeed rotary swaging tools, the reduction zone consisted of HS6-5-3C (wear-resistant, high friction) and the calibration zone of X110CrMoV8-2 or HS6-5-2C (fracture-resistant and highly micro-machinable), and the gradient zone was located between (see examples in Figs. 6.15 and 6.16).

Micro rotary swaging tools were manufactured in the hardened state by means of micro milling. The machining was carried out on a DMG Sauer Ultrasonic 20 linear machine tool. The machining operation comprised multiple consecutive roughing and finishing steps. CAD/CAM programming was used for tool path generation. In micro machining, the procedure of tool path generation is essential to achieve the desired shape accuracy and surface finish [Bri13]. Conventional path planning with a projected line pitch is not sufficient, as this would result in an inhomogeneous contour of the micro rotary swaging tools. In this study, the tool path generation was carried out with the line pitch arranged tangential to the targeted contour of the rotary swaging tools to meet the required machining quality. A detailed overview of all machining operations for the generation of the rotary swaging tool's micro contour can be found in [Cui17].
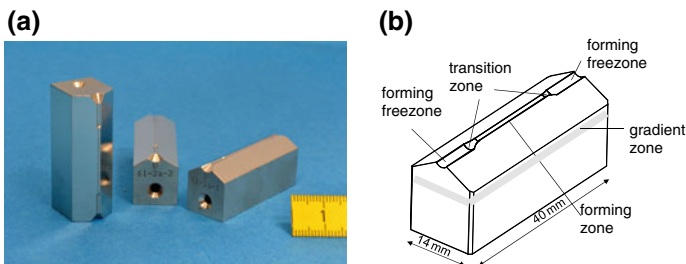

Fig. 6.15 Micro plunge rotary swaging tools of graded tool steel (X110CrMoV8-2/HS6-5-3C) processed by co-spray forming and hot deformation: **a** tool segments; and **b** different functional zones of the tools [Cui15]
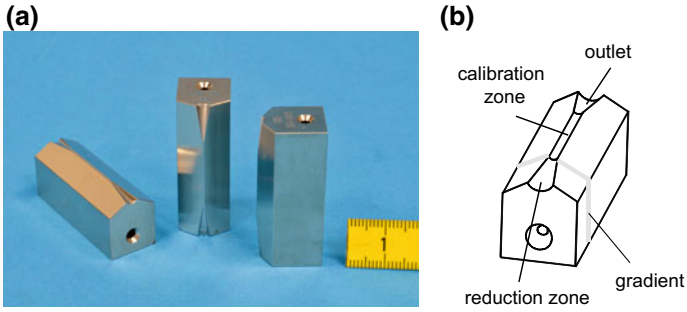
Fig. 6.16 Micro infeed rotary swaging tools of the graded tool steel (HS6-5-2C/HS6-5-3C) processed by co-spray forming and hot deformation: **a** tool segments; and **b** different functional zones of the tools

The functional surfaces of the forming tools after micro milling were investigated by means of scanning electron microscopy. Stereoscopic images were used to retrieve 3D information on the tool surfaces (using MeX software from Alicona), as seen in Fig. 6.17. It shows that the tool surfaces were smooth and the fine geometrical structures of the tools were precisely machined. Only slight traces of micro milling were observed at the tool surfaces. The excellent micro-machinability of the graded steels was guaranteed due to their fine and homogeneous microstructure.
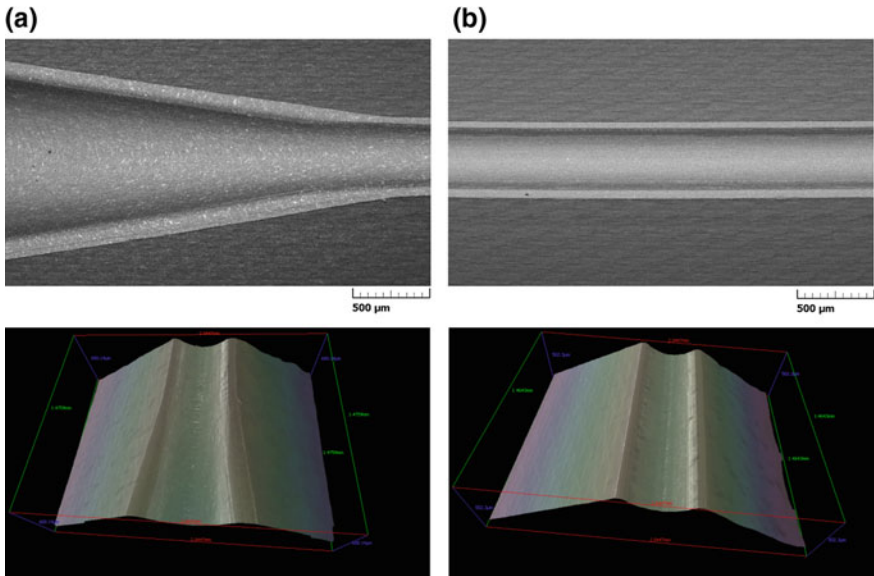

Fig. 6.17 Functional zones of a set of micro infeed rotary swaging tools (X110CrMoV8-2/HS6-5-3C) after micro milling: **a** reduction zone; **b** calibration zone

Refinement of the hard carbides by faster cooling during spray forming and more fracture of the carbides during heavier hot deformation would further improve the micro-machinability of the tool materials.

6.2.5 Performance of Micro Forming Tools

Rotary swaging is an incremental forming process for tubes, bars and wires. The workpieces are deformed in the swaging head by the forming tools (at least two segments), which rotate around the workpieces and perform radial oscillating movements at high frequency. There are two main variations of the process: plunge rotary swaging and infeed rotary swaging [Kuh08]. The diameter of the workpiece is reduced over the complete fed length during infeed rotary swaging, and it allows only local diameter reductions during plunge rotary swaging.

Sets of micro forming tools, which were fabricated from the graded tool steels, were tested in the micro rotary swaging machine (Type Felss HE 3/DE). Wires of stainless steel 1.4301 (AISI 304) in annealed state (surface hardness 300 HV0.1) were used for the test. The functional surfaces of the forming tools before and after the rotary swaging were investigated by means of scanning electron microscopy.

In plunge rotary swaging, the diameter of the stainless steel wires was reduced from 1.0 mm to the final diameter of 0.8 mm. The tool oscillated with a frequency of 100 Hz and the radial displacement was set to 35 µm/s. The total strain of the wires was 0.45. The gradient zone in the tool segments did not show signs of fracture or cracking after the test (up to 2500 pieces).
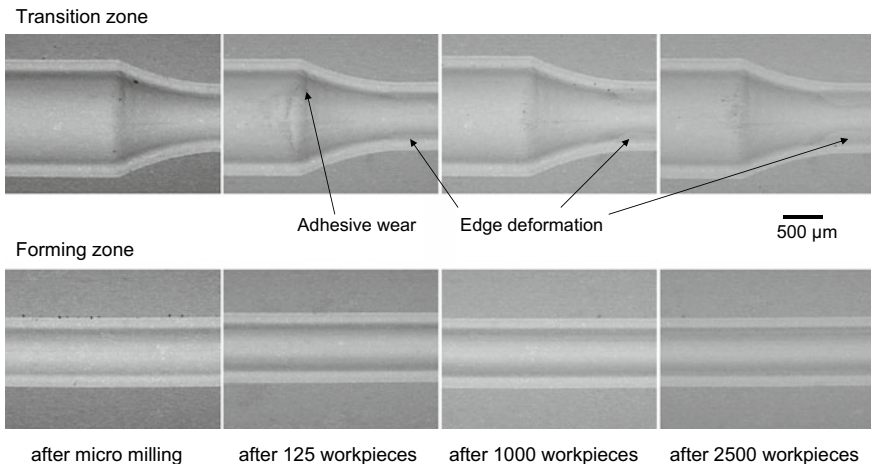

Fig. 6.18 Functional zones of the micro plunge rotary swaging tools before and after deforming workpieces of austenitic steel 1.4301 (forming zone Ø = 0.8 mm) [Cui15]

The functional surfaces of a forming tool segment (X110CrMoV8-2/HS6-5-3C) before and after micro rotary swaging are shown in Fig. 6.18. Slight adhesion of the workpiece on the tool surfaces and slight deformation/abrasive wear in the transition zone appeared. The forming zone of the tools was almost unchanged after processing 2500 workpieces. The shape, dimensional accuracy, and surface quality of the processed wires were satisfactory.

In infeed rotary swaging, the diameter of the stainless steel wires was reduced from 1.0 to 0.5 mm in one step, which corresponds to a total strain of 1.38. The tool oscillation took place with a frequency of 100 Hz and the workpiece axial feed velocity was 3 mm/s, which also means a displacement of 0.03 mm per stroke. The tools were investigated after forming wires of 5, 15, 35 and 85 m, respectively. The graded tool segments survived the test, and no fracture or cracking in the gradient zone was observed.

The functional surfaces of a forming tool segment (HS6-5-2C/HS6-5-3C) after micro infeed rotary swaging of AISI 304 wire of different lengths are shown in Fig. 6.19. The geometrical structures and the surface quality of the forming tools were not significantly changed by the swaging process. Slight abrasion in the reduction zone occurred after cold forming 5 m of wire. Slight adhesion of the wire on the tool surface was also observed both in the reduction zone and in the calibration zone. The abrasion and adhesion in the reduction zone are more pronounced than in the calibration zone since the loads (impact forces during swaging) and the friction between the wire and the tool were much higher in the reduction zone.

The degree of deformation and wear of the forming tools increased with the increasing number/length of workpieces. This might lead to poor surface roughness, low size and shape accuracy of the workpieces and even complete failure of the deformation (fracture of the workpieces). In order to reduce the deformation and
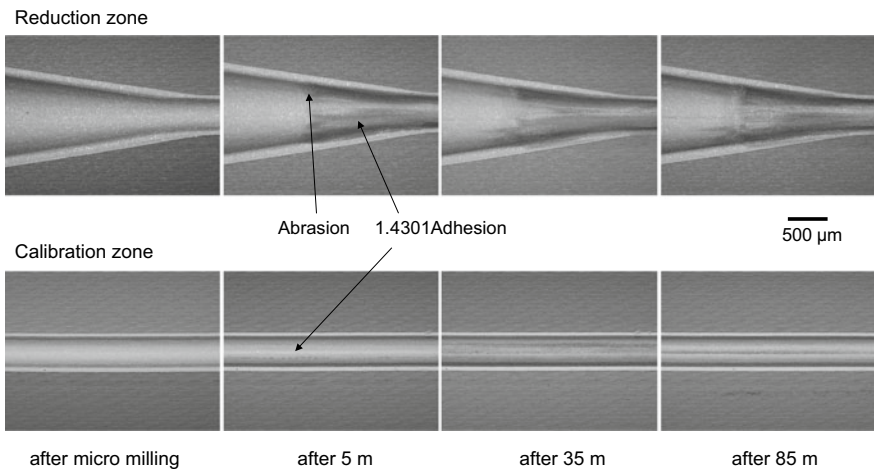

Fig. 6.19 Functional zones of the micro infeed rotary swaging tools before and after deforming workpieces of austenitic steel 1.4301 (forming zone Ø = 0.5 mm) [Cui16]

wear of the swaging tools, several strategies have been proposed to further improve the behavior of the swaging tools: (1) applying stronger tool materials in the tool surfaces, (2) reducing the deformation ratio of the workpieces, (3) reducing the temperature of the tools by coolant, and (4) improving the lubrication of the tools to reduce the friction between the workpieces and the tools.

6.3 Production of Thin Sheets by Physical Vapor Deposition

Andreas Mehner[*]**, Julien Kovac and Hans-Werner Zoch**

Abstract Thin metallic foils with thicknesses below 50 µm are required for the production of hollow micro components by deep drawing. The production of such foils by conventional metallurgical methods and cold rolling requires highly ductile materials such as pure aluminum, copper or stainless steel. Hardenable high-strength alloys are not available as thin foils due to the limited manufacturing process for such materials. Therefore, an alternative process based on physical vapor deposition (PVD) was developed in order to produce thin metallic foils with improved mechanical strength. The PVD-based production process and the micro structure and mechanical properties of the resulting thin metallic foils will be presented for several hardenable high strength aluminum alloys and steels. Selected foils were successfully tested for deep drawing of high-strength sub-millimeter micro cups.

Keywords Sheet metal · Composite · Physical vapor deposition (PVD)

6.3.1 Introduction

There is an increasing industrial demand for micro parts with enhanced mechanical properties and reliability. Micro deep drawing of submillimeter parts with complex shapes requires thin metallic foils with a thickness below 50 µm. Common metallic foils for deep drawing are produced by cold rolling of ductile materials such as pure aluminum, copper or stainless steel [Beh16]. These materials are characterized by high ductility and low mechanical strength. Although a few authors have investigated the drawability of some special high-strength materials [Had13], these materials are generally difficult to obtain as thin foils with a thickness below 50 µm because cold rolling of high-strength materials is very limited due to strain hardening, which requires a series of multiple cold rolling and annealing processes in order to restore the ductility of these materials after each cold rolling process.

Physical vapor deposition (PVD) and particularly magnetron sputtering have been proposed as an alternative process to produce thin foils of high-strength alloys [Sto10]. Such PVD thin foils were obtained by deposition of the considered materials onto substrate foils which were removed by chemical etching after the deposition process, in order to obtain freestanding thin foils. Research was necessary to find appropriate process parameters as well as a suitable method to separate the deposited films from the substrate foils. There are several methods to separate the deposited films from a substrate. Firstly, there is the use of non-adhesive substrates such as oxidized steel or the deposition of soluble

interlayers such as NaCl that easily dissolve in water after the deposition process [Mat02]. A second method is removing the substrate by etching. The etchant has to be selected carefully so that the coating material remains undamaged. Muggleton has provided a variety of appropriate substrates and etchants to produce thin freestanding PVD films for different materials [Mug87]. Instead of removing the metallic substrate foils, it is also possible to use PVD-coated substrate foils as bimetallic foils. The mechanical strength of the substrate foils made of conventional ductile materials such as pure aluminum, copper or austenitic stainless steel could be increased by the deposition of thin layers of high-strength aluminum alloys or martensitic steels, resulting in high-strength bimetallic foils. It was shown that some mechanical properties of bimetallic sheets or foils are deduced from rules of mixtures. Hence, for aluminum/stainless steel bimetallic sheets, the apparent elastic modulus, the tensile strength and the yield strength coefficient (according to Hollomon's law) follow rules of mixtures, whereas the uniform elongation and the strain hardening exponents are deduced by force weighted laws of mixtures [Lee88]. In each case, a significant increase of strength and ductility compared to pure aluminum was observed. The deep drawing behavior of aluminum/stainless steel bimetallic sheets was investigated by various authors. Parsa et al. investigated the evolution of the limit drawing ratio in single drawing and redrawing for bi-layered sheets with various layer ratios of aluminum and stainless steel through simulation and experiments [Par01]. They found that with increasing steel layer thickness (i.e. decreasing aluminum layer thickness) the limit drawing ratio increased. The limit drawing ratio also depends on the orientation of the sheets in the experimental setup. It was lower if the aluminum layer faced toward the punch.

Promising alloys for micro cold forming are high-strength aluminum alloys such as scandium- or zirconium-containing aluminum alloys. Aluminum–scandium alloys are used for several high tech applications, in particular in the construction of aircraft parts, where the combination of light weight and high strength is particularly important. Among the different alloying elements for aluminum alloys, scandium is the one that results in the best increase of hardness per fraction of element [Roy05]. Alloying aluminum with scandium leads to the formation of nanometer-scale spheroidal Al_3Sc precipitates which efficiently impede the motion of dislocations due to their high coherency with the aluminum matrix and their high dispersivity. The Al_3Sc precipitates increase the mechanical strength, hardness and also the recrystallization temperature of these alloys. It was also shown that the addition of scandium improves the corrosion resistance and weldability of these alloys. A possible way to reduce the price of these alloys is partial substitution of the rare and expensive scandium by zirconium, which is much less expensive. In thermodynamic equilibrium, aluminum–zirconium alloys contain Al_3Zr precipitates with a tetragonal lattice structure which are less coherent with the aluminum matrix compared to Al_3Sc, resulting in limited reinforcement [Mur92]. However, during heat treatment, metastable cubic Al_3Zr precipitates form primarily and the tetragonal equilibrium phase only appears after long annealing times [Kni08]. The metastable cubic Al_3Zr precipitates have similar properties to those of the Al_3Sc precipitates and thus also increase the mechanical strength, though a little less than

scandium. Another issue of aluminum–scandium alloys is that the size of the precipitates rapidly increases. Beyond a critical radius, they become incoherent, resulting in a decrease of hardness. In order to overcome this issue, aluminum alloys containing both scandium and zirconium were developed. As a result, small amounts of zirconium are incorporated into Al_3Sc precipitates. $Al_3(Sc_{1-x}Zr_x)$ precipitates are more stable and coarsen more slowly due to the reduced diffusivity of Zr in aluminum [Ful05]. Moreover, a substantial increase of strength has been reported for Al–Sc–Zr alloys compared to pure Al–Sc alloys [Son11].

6.3.2 Methods

6.3.2.1 The Magnetron Sputtering Process

In the following, the PVD magnetron sputtering process to produce thin Al–Sc–Zr foils will be presented. Magnetron sputtering is a physical vapor deposition (PVD) process for the deposition of thin films or coatings. The most common applications are the deposition of hard coatings for cutting and forming tools, hard coatings for wear and corrosion protection, low friction coatings, conducting and semi-conducting thin films for microelectronic devices, and photovoltaic cells or special coatings for medical applications. Sputtering is based on the evaporation of target materials by low-pressure plasmas. The vaporized target materials condense onto the substrates and also on the walls of the vacuum chamber. The sputtering process is performed in a vacuum chamber. After evacuation to about 10^{-6} mbar residual pressure, an inert gas (usually argon, neon or xenon) is introduced into the chamber until a working pressure of about 10^{-3} mbar is achieved. The metallic targets are connected to the cathode of a generator with a negative voltage of several hundreds of volts, whereas the rest of the chamber and the substrate are electrically grounded. A low-pressure plasma is created in front of the target due to collision ionization of the inert gas atoms by accelerated electrons emitted from the cathode (target). The positively charged inert gas ions created, such as Ar^+, are accelerated into the direction of the negatively charged target and hit with high kinetic energy onto the target where the surface atoms are sputtered (evaporated). The sputtered atoms move in the opposite direction to the substrate and progressively form a coating. Magnetron sputtering is an advanced sputtering process using permanent magnets behind the targets in order to concentrate the low-pressure plasma in front of the target, which increases the sputter and deposition rate [Tho86]. A more detailed description of the process can be found in reference books such as those of Matox [Mat02] or Ohring [Ohr02].

For conventional direct current magnetron sputtering, the maximum plasma power density is limited due to the formation of arcs if the plasma power density exceeds approx. 25 Wcm^{-2}. The risk of arc formation is reduced if the plasma power is pulsed. Pulsed DC magnetron sputtering (DCMS) allows an increase of the maximum plasma power density up to approx. 50 Wcm^{-2}. For pulsed DCMS,

the duration of the pulse and off-cycle are comparable. The pulse frequency is in the range from 20 to 70 kHz. High-power impulse magnetron sputtering (HiPIMS) was developed for a further increase of the plasma power density [Sar10]. For HiPIMS, the duration of the power pulse is much shorter than the duration of the off-cycle. The duty cycle is defined as the ratio of the duration of the pulse to the duration of the whole cycle. For HiPIMS, the duty cycle is typically between 1% and 20%. For low-duty cycles, the power density could be increased up to 1000 Wcm^{-2}. For example, in a HiPIMS process with a defined frequency of 1000 Hz, a duty cycle of 0.2 ms (20%) and an average power of 2 kW, the maximum peak power could be increased up to 10 kW. The principal advantage of HiPIMS is the higher kinetic energy of the sputtered atomic species, resulting in a higher film density and better adhesion to the substrate [Mül87].

6.3.2.2   Separation of the Foils from the Substrate

For the production of freestanding metallic foils, it is necessary to separate the coated material from the substrate foil. This separation step is not required for the production of bimetallic PVD foils, since the substrate foils remain as a component of the bimetallic foils. For the production of freestanding monometallic aluminum foils by chemical etching, however, an appropriate choice of the substrate material is required. For the production of PVD aluminum alloy foils, low alloyed ferritic steel substrate foils like DC01 are adequate since these steels easily dissolve in concentrated nitric acid, whereas the aluminum alloys remain undamaged during the etching process due to their high corrosion resistance. For the production of freestanding PVD-steel foils, the use of thin copper substrate foils is appropriate because copper can be removed using an etching solution of ammonia and tri-chloroacetic acid, which does not attack the resulting steel foil [Mug87].

6.3.2.3   Continuous PVD Coating Process for Thin Substrate Foils

For mass production of bimetallic PVD foils, a continuous PVD magnetron sputtering process is required. A prototype device for continuous physical vapor deposition of thin metallic substrate tapes in an industrial PVD magnetron sputtering unit (CemCon 800/CC) was developed, constructed and tested. Figure 6.20 shows the scheme for continuous PVD magnetron sputtering in a PVD vacuum chamber with six targets. During the coating process, the metallic substrate tape from a donor coil is transported in front of the six targets. The coated tape is wound onto a receiver coil. The substrate tape is led by pulley rolls. For the practical realization, a substrate tower device was designed, as shown in Fig. 6.20b. A synchronic wind-off and wind-up of the substrate tape from the donor coil to the receiver coil is achieved by a central gear wheel which drives the gear wheels of both coilers. The pulley rolls were equipped with tension springs in order to control the tension of the substrate tape.
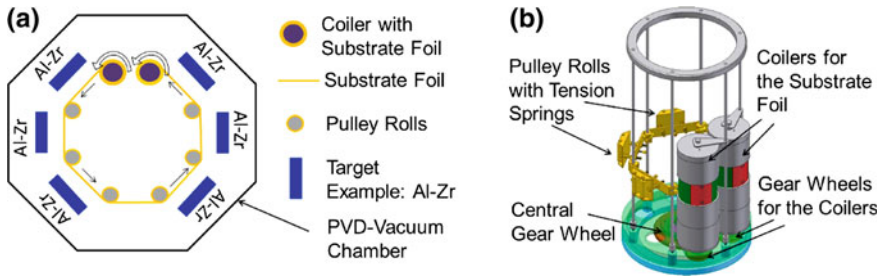
Fig. 6.20 Scheme of continuous magnetron sputtering in a PVD vacuum chamber (**a**). Design drawing of the constructed substrate tower for continuous PVD coating of long substrate tapes (**b**)

The deposited foil thickness is inversely proportional to the band uncoiling speed and it is directly proportional to the target number, the plasma power and the exposition length of the band between the two coils. As a result, in practice a higher band speed will lead to smaller thickness. Producing thicker foils requires a slowdown of the band speed or an increase of the deposition rate. With the current unit, the maximum exposition length is limited to about one meter. Producing Al–Sc–Zr/steel bimetallic foils with a layer thickness of 5 µm, for instance, would require a band speed of 36 mm/min. As a result, the production of 100 m of this foil would take about 2 days.

6.3.3 Results for PVD Al–Sc, Al–Zr and Al–Sc–Zr Thin Foils

Scandium and zirconium alloyed aluminum thin foils were produced in different types of magnetron sputtering units, which also influenced their structural and mechanical properties. Firstly, a laboratory-scale unit equipped with a single target and a non-moving substrate holder was used. Here, the substrate temperature was kept constant with a heating/cooling system. Secondly, an industrial PVD unit equipped with four or six targets and a rotating substrate holder was used for the production of larger foils.

6.3.3.1 Results for Al–Sc, al–Zr and Al–Sc–Zr Thin Foils Produced in a PVD Unit with Fixed Substrate Holder and Controlled Substrate Temperature

In the PVD unit with a non-moving substrate holder and a single target, the angular flow of atoms impinging onto the substrate follows a cosine law [Ohr02], resulting in an inhomogeneous distribution of the film thickness, as shown in Fig. 6.21a. Nonetheless, the flow of atoms is particularly strong and results in a very

close-packed columnar structure as shown in Fig. 6.21b and c. The deposition process results in non-equilibrium thermodynamic conditions due to the quick condensation of energetic gaseous species onto a cold substrate (below 40 °C). The result of these conditions is an oversaturated aluminum solid solution, nearly free of precipitates [Kov13].

The mechanical properties of PVD–Al–Sc, Al–Zr, and Al–Sc–Zr thin foils were studied by tensile tests. The chemical composition of the target materials and of the produced PVD foils was measured by spark optical emission spectroscopy (S-OES) and by glow discharge optical emission spectroscopy (GDOES). The PVD–Al–Sc foils contained 2.0 mass% scandium, the PVD–Al–Zr foils contained 4.0 mass% zirconium and the PVD–Al–Sc–Zr foils had 1 mass% scandium and 0.5 mass% zirconium.

Several rectangular tensile test specimens were cut from each foil variant. In Fig. 6.22, selected representative tensile curves for each variant show the impact of the target power, the substrate temperature and a post-deposition heat treatment on the mechanical properties of the resulting Al–Sc, Al–Zr and Al–Sc–Zr foils. The foils have different tensile characteristics. Al–Sc foils show tensile strengths up to 400 MPa and high elongations at fracture up to approx. 10%. In comparison, the tensile strength of Al–Zr foils is higher but the elongation at fracture does not exceed 2%. Al–Sc–Zr foils achieved the highest strength but are more ductile than Al–Zr foils.

The experimental results show that the target plasma power, the substrate temperature as well as post annealing have a significant influence on the mechanical strength of the different foils. When the target plasma power is increased, the
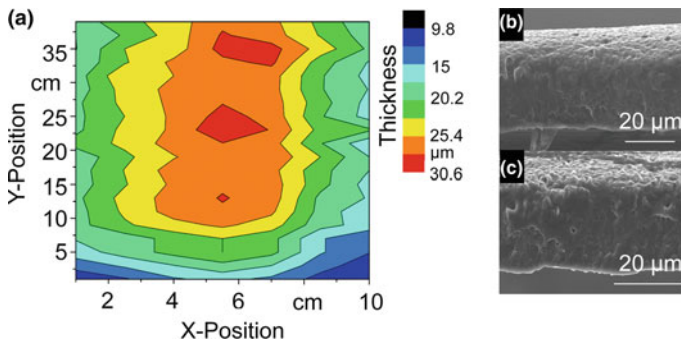

Fig. 6.21 Spatial distribution of the film thickness for an Al–Sc–Zr foil produced with a non-moving substrate holder and a single Al–Sc–Zr target (plasma power 1 kW) after 3.5 h of deposition (**a**). SEM pictures of the cross-sections of a PVD Al–Sc foil (**b**) and a PVD Al–Zr foil (**c**) produced with a non-moving substrate holder and a single target (plasma power 2 kW)
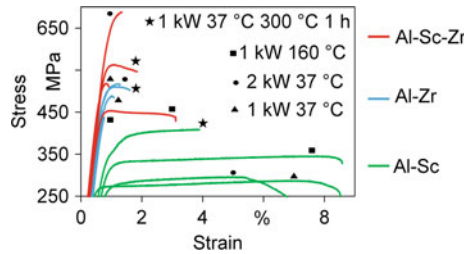
Fig. 6.22 Selected tensile curves of PVD Al–Sc (2 mass-% Sc), Al–Zr (4 mass-% Zr) and Al–Sc–Zr (1 mass-% Sc + 0.5 mass-% Zr) foils produced with target powers of 1 and 2 kW and substrate temperatures of 37 and 160 °C with and without post-deposition heat treatment at 300 °C for 1 h in normal air atmosphere

sputtered atoms hitting onto the substrate have higher kinetic energy. Due to momentum transfer, the surface atoms on the coating gain a higher mobility, which induces less porosity [Mül87]. The high kinetic energy of the sputtered atoms also increases the density of crystal defects as dislocations [Ohr02], which increase the mechanical strength of the foils. With increasing substrate temperature, different effects occur. A higher temperature may activate precipitation and generates thermal stress, which increases the strength. But also dynamic defects recovery is activated, which decreases the strength. The mechanical strength may thus increase or decrease, depending on the competition of these effects. During the post heat treatment at 300 °C, diffusion of the alloying elements occurs, resulting in the formation of precipitates and thus increasing the strength. However, recovery may also occur, which compensates the rise of the strength as observed for PVD Al–Zr foils produced at respectively 2 and 3 kW and aged at different temperatures for various times [Ego16].

PVD Al–Sc and Al–Zr foils deposited at substrate temperatures of 37 °C and 160 °C were tested by deep drawing with a constant blank holder pressure of 1 N/mm^2 [Beh12]. For Al–Sc foils, the limiting drawing ratio (LDR) was always 1.6, independently of the substrate temperature. For the Al–Zr foils, higher LDRs of 1.7 and 1.8 were reached for foils deposited at 160 and 37 °C. The higher LDR of the Al–Zr foils may be a consequence of the higher mechanical strength of these foils (Fig. 6.22).

6.3.3.2 Results for Al–Sc–Zr Foils Produced in a PVD Unit with Multiple Targets and Rotating Substrate Holder

The main disadvantage of a single target and non-moving substrate configuration is the limited size (110 × 500 mm^2) of the foils and an inhomogeneous thickness distribution, as shown in Fig. 6.21. Larger foils with a homogeneous thickness distribution were obtained using a magnetron sputtering unit with a rotating substrate holder and multiple targets, as shown in Fig. 6.23a. The consequence of this

configuration is a lower average flow of sputtered atoms with a lower kinetic energy. If the rotating substrate holder and multiple targets are used, the flow of sputtered atoms and their kinetic energy varies periodically in time. The time-averaged value of the flow of sputtered atoms and their average kinetic energy was lower for experiments in the PVD unit with rotating substrate holders, which leads to a notable drop of the deposition rate. An averaged deposition rate of approx. 5.7 μm/h was measured for the experiments using the PVD unit with a single DC target with 1 kW plasma power and a non-moving substrate holder. For the PVD unit with four targets (each 1 kW plasma power) and a rotating substrate holder, the measured deposition rate was approx. 3.0 μm/h, with much better homogeneity of the thickness distribution, as shown in Fig. 6.23b.

Al–Sc–Zr foils were produced using a PVD unit with a rotating substrate holder and with three DC Al–Sc targets (2 mass% Sc) and one DC Al–Zr target (2 mass-% Zr) or with two HiPIMS Al–Sc–Zr targets (1 mass-% Sc, 0.5 mass-% Zr) [Kov18]. The DC target plasma power was 2 or 4 kW. The morphology and the mechanical properties of these foils were compared to foils produced by HiPIMS using an averaged target power of 2 kW (duty cycle 20%) at a frequency of 1000 Hz. The scandium and zirconium content of the foils was measured by glow discharge optical emission spectroscopy (GDOES). Both DC Al–Sc–Zr foils contained 1.8 mass-% Sc and 0.3 mass-% Zr. The HiPIMS Al–Sc–Zr foil contained 1.8 mass-% Sc and 0.6 mass-% Zr. Figure 6.24 shows SEM and optical microscopy pictures of the cross-sections of all three foils. All foils showed surface porosities resulting from shadowing effects during the PVD process. These shadowing effects increase with the rising film thickness. The porosity increased with decreasing kinetic energy of the deposited atoms. This is because the mobility of the surface atoms on the coating is reduced and pores are less likely to be filled [Mül87]. Thus, an increase of the DC power or using HiPIMS results in fewer and smaller pores, as shown in Fig. 6.24.
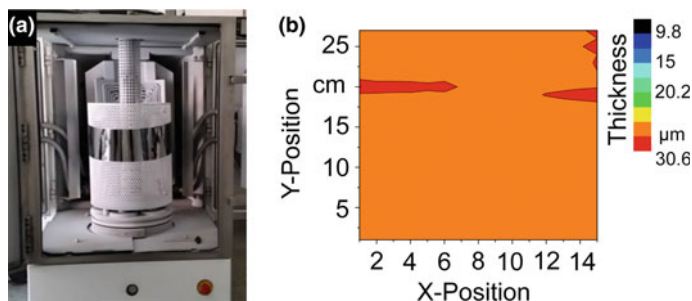

Fig. 6.23 Macro image of a polished steel foil substrate in the PVD unit with rotating substrate holder (**a**) and a plot of the resulting thickness distribution for a PVD Al–Sc–Zr foil produced in this PVD unit (**b**)
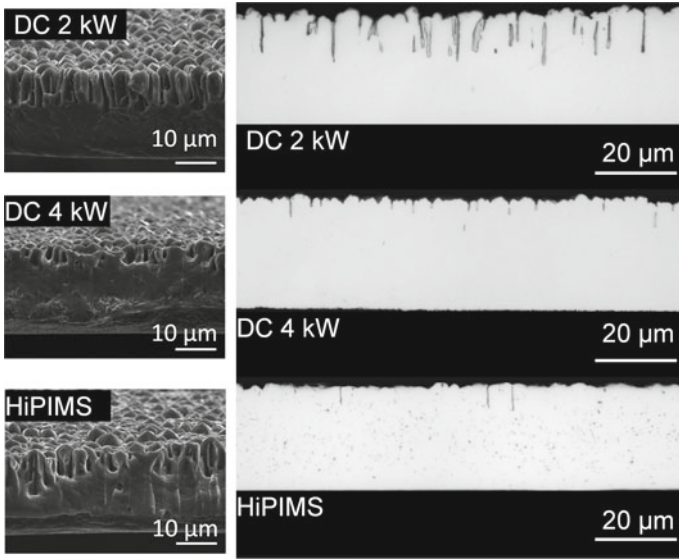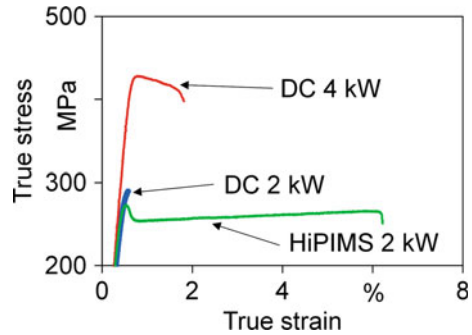
Fig. 6.24 SEM pictures of the free surface of freestanding Al–Sc–Zr foils and optical microscopy pictures of the cross-sections of these foils

Table 6.2 Average Young's modulus, yield strength ($Rp_{0.01}$), tensile strength (Rm) and strain at fracture (A) of Al–Sc–Zr monometallic foils

Al–Sc–Zr foil	E (GPa)	$Rp_{0.01}$ (MPa)	Rm (MPa)	A (%)
2 kW DC	58 ± 4	269 ± 42	292 ± 63	0.6 ± 0.2
4 kW DC	69 ± 2	314 ± 29	400 ± 38	1.5 ± 1.3
2 kW HiPIMS	65 ± 1	230 ± 9	260 ± 12	5.7 ± 3.9

The results of tensile tests with Al–Sc–Zr foils deposited using DCMS with different target powers and HiPIMS showed that the microstructure and the morphology of the foils have a great impact on their mechanical properties. The Young's modulus (E), the ultimate tensile strength (Rm), the yield strength at 0.01% strain ($Rp_{0.01}$) and the elongation at fracture (A) were determined by 10 tensile tests for each variant. The results are summarized in Table 6.2. Selected tensile test curves are shown in Fig. 6.25. The low Young's modulus of 59 MPa and the low strain at fracture of 0.7% for the DC Al–Sc–Zr foil at 2 kW target power compared to those of the 4 kW DC and the 2 kW HiPIMS foils are related to the high surface porosity of this foil, as shown in Fig. 6.24. The yield strength and the tensile strength of the Al–Sc–Zr foils produced in the PVD unit with the moving substrate holder were lower than for the foils produced in the PVD unit with the static substrate holder shown in Fig. 6.22. This effect may be the result of a higher average kinetic energy of the hitting atoms for the latter foils. Similar to the foils

Fig. 6.25 Selected tensile
test curves of the different
Al–Sc–Zr foils

produced with the static substrate holder, an increase of the DC plasma target power
from 2 to 4 kW results in an increase of the yield and tensile strength, whereas the
2 kW HiPIMS deposited foil showed comparable strength to that of the 2 kW DC
foil.

   The results of micro deep drawing with freestanding PVD Al-Sc-Zr foils depend
on the orientation of the foil facing the die. This orientation effect is due to the
different surface morphologies of the top side compared to the bottom side which
was in contact with the substrate foil, as shown in Fig. 6.24. On the top side (upper
side or free surface), the columnar grains grow freely, resulting in high roughness
and porosity. If the free surface of the foils faced towards the die, the LDR was only
1.7, whereas a LDR of 1.8 was reached if the bottom side faced toward the die
[Kov18]. This is because strong tensile stress always develops on the outer shell of
the cup. Due to pores (Fig. 6.26b), the free surface is expected to sustain less stress,
resulting in crack formation for lower drawing ratios compared to the denser bottom
surface (Fig. 6.26a). Thus, higher LDRs are achieved if the bottom surface faces
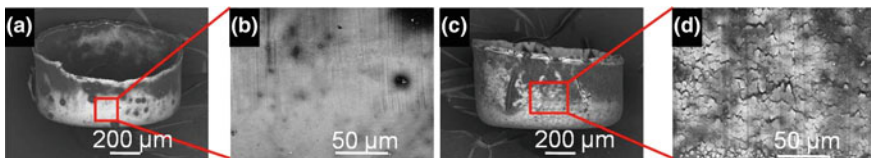towards the die.

Fig. 6.26 SEM pictures of Al–Sc–Zr cup obtained by deep drawing with drawing ratio of 1.7
with the free surface facing toward the punch (inside) (**a, b**) and with the free surface facing toward
the die (**c, d**)

6.3.4 Results for PVD Al-Sc-Zr/Stainless Steel Bimetallic Foils

The mechanical properties and the drawability of high-strength PVD Al–Sc–Zr foils were further improved by combination with more ductile but lower strength austenitic stainless X5CrNi18-10 steel foils. The mechanical properties of bimetallic foils or complex laminates are typically described by rules of mixtures, stating that the mechanical properties of laminates are averaged values of the properties of the constituting compounds weighted by their volume fraction. Hence, bimetallic Al–Sc–Zr/X5CrNi18-10 foils are expected to show strength and ductility intermediate between that of pure Al–Sc–Zr foils and X5CrNi18-10, depending on the thickness of each layer. The rule of mixtures was studied by depositing 5, 10 and 15 μm thick layers of Al–Sc–Zr onto thin commercially available X5CrNi18-10 foils with thicknesses of 25, 20 and 15 μm so that the total thickness of the resulting bimetallic foil was always 30 μm. The X5CrNi18-10 substrate foils (width 50 mm) were fixed to the rotating substrate holder as described in Sect. 6.3.3.2. A DC target power of 4 kW was used. Figure 6.27 shows typical tensile tests curves of the different bimetallic foils and of a freestanding Al–Sc–Zr foil and a commercial X5CrNi18-10 foil. The average values and standard deviations of the measured tensile properties are given in Table 6.3.

The measured strength and ductility of the bimetallic foils was between those of the monolayer Al–Sc–Zr and X5CrNi18-10 foils. All the bimetallic foils showed higher yield and tensile strength compared to the monometallic Al–Sc–Zr foils. The elongation at fracture was comparable to monometallic stainless steel foils. These properties also increased with the layer thickness (volume fraction). The yield and tensile strength as well as the apparent Young's modulus of the bimetallic foils are well predicted by rules of mixtures [Kov18]. Despite being submitted to higher strains than the elongation at fracture of monometallic Al–Sc–Zr foils, the Al–Sc–Zr layer in the bimetallic foils did not crack prematurely in the tensile tests. Thus, the bimetallic foils behaved similarly to non-composite materials. According to Choi et al. [Cho97], the impressive augmentation of strength and ductility is related
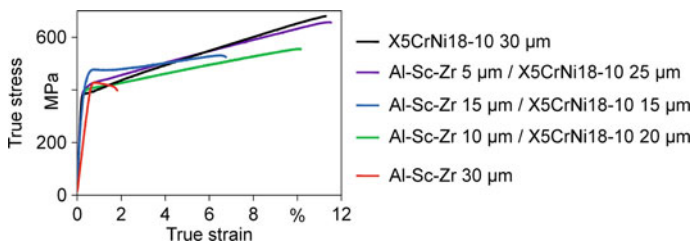

Fig. 6.27 Selected tensile test curves of bimetallic Al–Sc–Zr/X5CrNi18-10 foils with different Al–Sc–Zr layer thickness, of 30 μm thick monometallic Al–Sc–Zr and X5CrNi18-10 foils

Table 6.3 Average Young's modulus, yield strength (Rp0.01), tensile strength (Rm) and elongation at fracture of Al–Sc–Zr/stainless steel bimetallic foils and of Al–Sc–Zr and X5CrNi18-10 monometallic foils

Foil type	Thickness (µm) Al–Sc–Zr/ X5CrNi18-10	E (GPa)	$Rp_{0.01}$ (MPa)	Rm (MPa)	A (%)
Al–Sc–Zr	30/0	69 ± 2	314 ± 29	400 ± 38	1.5 ± 1.3
Bimetallic	15/15	148 ± 25	329 ± 43	526 ± 21	11.1 ± 8
Bimetallic	10/20	177 ± 14	327 ± 9	548 ± 10	12.1 ± 3
Bimetallic	5/25	192 ± 8	339 ± 12	662 ± 22	12.6 ± 1.1
X5CrNi18-10	0/30	197 ± 25	355 ± 13	684 ± 41	11.5 ± 1.8

to the wrapping of the bimetallic foils during tensile tests, due to the different lateral contraction of steel and aluminum.

The micro deep drawing experiments showed that the increase of ductility and strength observed in the tensile tests also resulted in better drawability. Indeed, whereas monometallic PVD Al–Sc–Zr foils achieved a limiting drawing ratio (LDR) of either 1.7 or 1.8, depending on the side facing towards the matrix, bimetallic foils of 25 µm of stainless steel and 5 µm of Al–Sc–Zr achieved a LDR of 1.9, independently of the orientation of the bimetallic foils in the drawing die [Kov18].

6.3.5 Production of Monometallic and Bimetallic Steel Foils

The production of thin steel foils by magnetron sputtering is more challenging than the production of thin aluminum alloy foils. Firstly, ferromagnetic steel targets such as ferritic chromium steels (X40Cr13) shield the magnetic field of the magnetron targets, resulting in a less concentrated plasma in front of the steel target, which reduces the sputter and the deposition rate. Secondly, the melting point of steels is higher than that of aluminum alloys, resulting in reduced surface diffusion, which supports the formation of pores in the foils [Kov13a]. Furthermore, austenitic steels may present an unexpected metastable ferrite structure after magnetron sputtering if the substrate temperature is low [Dah70], and the steel deposit may also be over-saturated in crystal defects such as dislocations or point defects, resulting in particularly brittle foils. Therefore, heat treatment of the foils may be necessary to reduce the density of crystal defects and improve the ductility of the PVD steel foils [Kov16]. Despite these constraints, PVD steel foils with promising properties were successfully produced by magnetron sputtering, as shown in the following.

The first example are high manganese austenitic X5MnSiAl25-3-3 steel foils. This steel belongs to the group of TWIP steels (TWIP: twinning-induced plasticity) which are characterized by very high ductility due to the TWIP effect. The austenite

lattice structure of this steel is characterized by a relatively low stacking fault energy, which enables twinning as the dominant plastic deformation mechanism. Because of the TWIP effect, the tensile strength and elongation at fracture of these alloys are much higher than those of conventional stainless steels. For the X5MnSiAl25-3-3, a tensile strength of up to 800 MPa and an elongation at fracture of 90% were reported [Grä00]. Therefore, this steel is interesting for the deep drawing of micro components with a high limit drawing ratio and strength. But the deposition of X5MnSiAl25-3-3 foils by magnetron sputtering resulted in foils with relatively high porosity and brittleness. Therefore, it is important to reduce the residual porosity by increasing the plasma target power and by biasing the substrate [Kov13a]. Also, using mirror polished substrate foils contributed to lowering the shadowing effects responsible for porous structures [Kov17]. Following these adjustments, denser and smoother deposits were obtained. Nevertheless, after the deposition, the foils still showed high brittleness due to a fine-grained structure, a high density of crystal defects and a ferritic instead of an austenitic lattice structure. Therefore, an annealing process was required in order to obtain a fully austenitic recovered and recrystallized structure [Kov16]. Prior to the annealing process, the copper substrate foils were removed by etching as described in Sect. 6.3.2.2. The microstructure and the mechanical properties of magnetron sputtered X5MnSiAl25-3-3 foils after annealing at different temperatures are presented in Fig. 6.28a and b. Foils treated at low temperatures (500–600 °C) presented a finely grained phase mixture of austenite and ferrite with high tensile strength (>1100 MPa) but low ductility (1%). Only after annealing at high temperature (800 °C), the foils achieved a coarse-grained austenitic structure. The strength decreased to approx. 750 MPa, which is higher than that of X5CrNi18-10 foils, but their ductility was quite comparable to X5CrNi18-10 foils of the same thickness. But the maximum elongations at fracture of up to 90% as reported for the bulk materials [Grä00] were not achieved.

Another example of bimetallic foils which could be used for the production of high-strength micro components, are bimetallic foils of martensitic hardenable high carbon chromium steel (X75Cr17) onto ductile austenitic steel (X5CrNi18-10). The combination of these materials allows a good compromise between high strength and ductility. However, it was observed that the deposited X75Cr17 layers fail at low strains (<1%) during tensile tests and that the strength of the bimetallic foils was below the strength of monometallic X5CrNi18-10 foils. This behavior can be explained by the more similar contraction of both steel layers, preventing wrapping during deformation [Cho97], but also by the high brittleness of the X75Cr17 resulting from the fine grain structure and porosity. Small improvements of the tensile strength, ductility and critical strain (i.e. the strain at which the X75Cr17 layer begins to crack) of the bimetallic foils were reached by decreasing the X75Xr17 layer thickness and by application of a substrate bias voltage [Kov17a]. Nonetheless, the only way to obtain a higher tensile strength than pure stainless steel foils is annealing of the bimetallic foils. As shown in Fig. 6.28c and d, after
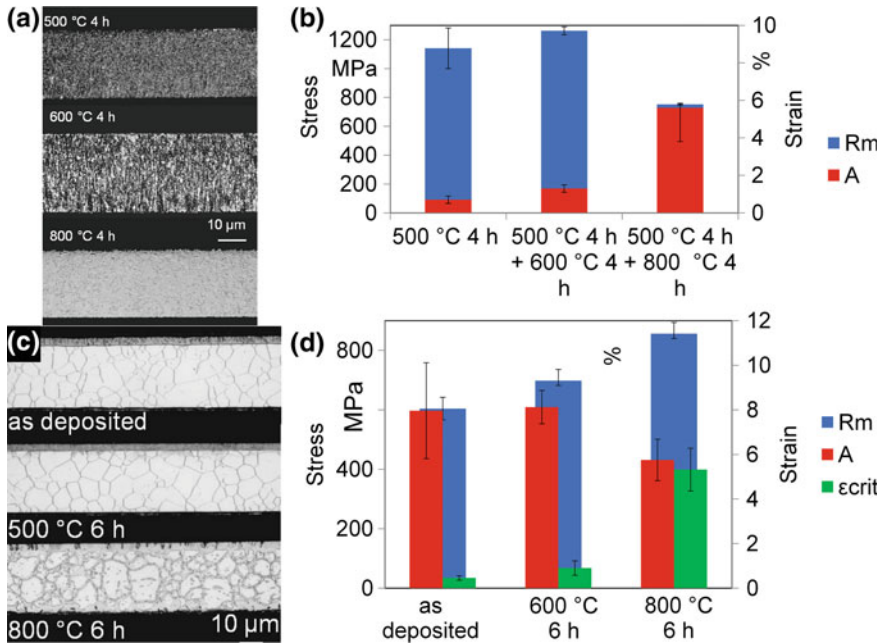
Fig. 6.28 Light microscopic pictures of the cross-sections and average tensile properties of X5MnSiAl 25-3-3 TWIP steel foils (**a**, **b**) and X75Cr17/X5CrNi18-10 bimetallic foils (**c**, **d**) after annealing at different temperatures

annealing at 500 °C the X75Cr17 foils failed at a critical strain of 0.9% and the strength of the bimetallic foil reached 700 MPa, which was slightly above that of the X5CrNi18-10 substrate foils. After annealing at 800 °C, no fracture of the X5Cr17 foil was observed during tensile tests and the strength reached by the bimetallic foil was above 850 MPa, whereas an appreciable strain at fracture of 5% was measured. This increase of tensile strength may, however, be partially due to carbon diffusion from the X75Cr17 coating to the X5CrNi18-10 substrate foil, resulting in a phase mixture of ferrite and austenite similarly to duplex steels. The drawability of these bimetallic foils was tested by micro deep drawing tests. Different limiting drawing ratios were obtained, depending on the orientation of the bimetallic foils to the drawing die. If the smooth X5CrNi18-10 substrate foil faced towards the die, a LDR of 1.8 was reached. If the brittle X75Cr17 layer faced towards the die, the micro cups failed more easily and the maximum LDR was only 1.7.

6.4   Heat Treatment of Micro Semi-finished Products and Micro Cold Formed Components

Anastasiya Toenjes[*]**, Axel von Hehl and Hans-Werner Zoch**

Abstract Heat treatment is an elementary process step in the production of metallic components. It serves on the one hand to adjust the formability of the semi-finished components by annealing processes and on the other hand to optimize the functional properties, for example, in terms of strength and hardness. An exactly adjusted heat treatment is particularly crucial for parts with thin wall thicknesses of less than 100 μm, since here the number of grains in the transverse section is low and thus weak points or defects have a considerably bigger impact on the failure behavior of components on the micro than on the macro scale [Köh10]. Besides, aspects such as handling and charging have to be considered particularly in the transfer of conventional processes from the macro to the micro scale. Thus, for the heat treatment of micro components, a new facility to carry out the heat treatment during falling was designed to avoid deformations during charging and processing of the sensitive components. This 5.5 m high drop-down tube furnace enables a variety of heat treatment processes for micro components made of both steel and aluminum alloys. In this regard, a wide range of macro processes could be scaled down to micro processes tailored to the drop-down tube furnace. Thus, recrystallization annealing, hardening, tempering, nitriding as well as age hardening can be performed during falling.

Keywords Heat treatment

6.4.1   Annealing Processes

The formability of a metal decreases with the increasing degree of deformation, which can be traced back to a rising dislocation density. Dislocations that occur during cold forming are carriers of plastic deformation. Due to their increasing number and interaction, however, they simultaneously impede further plastic deformation. Local stress fields of the dislocations superimpose during their interaction, leading to an increase of the macroscopic stress that must be overcome in order to uphold further plastic deformation [Eck69].

In order to recover the formability for further cold forming operations, heat treatment processes such as recrystallization annealing can be carried out for both steel and aluminum alloys. The aim of the process is to undo work hardening associated with cold forming and to restore plastic formability. In the recrystallization mechanisms, a distinction is made between primary recrystallization, secondary (/ternary) recrystallization, strain-induced grain boundary movement, and general grain growth [Eck69].

The primary recrystallization of a metallic structure requires a sufficient amount of cold forming (critical forming ratio) before heating above the recrystallization temperature, which corresponds to about 0.4 of the melting temperature of the material in Kelvin. Both the recrystallization temperature and the critical deformation degree are material-dependent factors. During recrystallization, high-angle grain boundaries begin to move through the material and eliminate dislocations that were formed during plastic deformation. The primary recrystallization is a rapid process compared to the other softening mechanisms, and generates a fully new microstructure with minimized dislocation density and renewed grain size. The resulting grain size is mainly dependent on the degree of deformation. The higher the degree of deformation, the smaller the grain size after recrystallization annealing [Eck69].

Recrystallization annealing can also be carried out during very short time cycles, benefiting the heat treatment of cold formed micro components. This can be seen from the example of the rotary swaged wire sections made of X5CrNi18-10. After a short-time heat treatment in the drop-down tube furnace at 1300 °C, the hardness can be reduced to less than 4 s by about 4250 H_{iT} 0.01/10/10/10 (Fig. 6.29). In addition, relationships between the degree of deformation, the temperature, the heat treatment time and the hardness are clearly visible [Bar12].

At the drop-down tube furnace temperature of 1300 °C, the recrystallization of the samples with a deformation degree of 3.22 is completed in just a few seconds. Figure 6.30a shows the microstructure of the sample after rotary swaging. After 1.3 s a new grain formation can be seen, but the old elongated structures have not completely disappeared (Fig. 6.30b). After 2.3 s, a completely new formation of
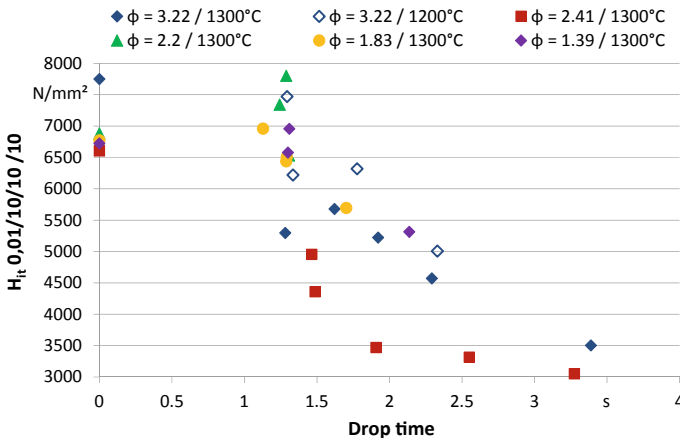

Fig. 6.29 Results of the universal micro hardness measurements indentation hardness versus drop time depending on the drop-down tube furnace temperature and the degree of deformation [Bar12]
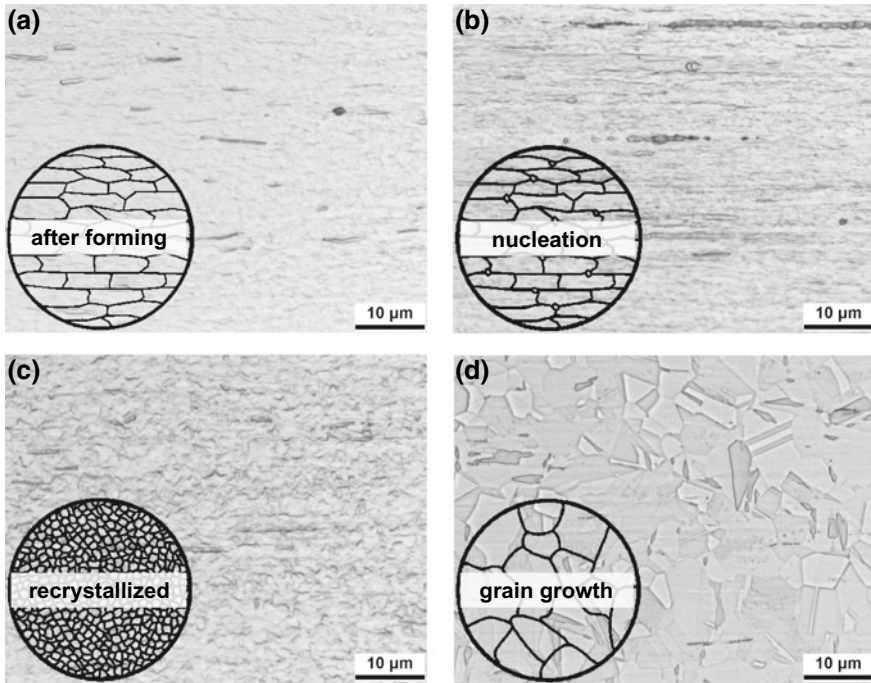
Fig. 6.30 Microstructure of a specimen after rotary swaging with $\varphi = 3.22$ **a** after forming and after subsequent short-time recrystallization annealing at 1300 °C for **b** 1.3 s, **c** 2.3 s and **d** 3.4 s; etched with V2A etchant for 120 s at 40 °C. Material: X5CrNi18-10 [Bar12, Sei14]

the grain structure with a grain size in the range of a few micrometers can be seen (Fig. 6.30c). Even after 3.4 s, a homogeneous grain growth occurs with the resulting grain sizes between 5 and 10 µm (Fig. 6.30d) [Bar12].

6.4.2 Martensitic Hardening of Steels

The aim of hardening is a considerable increase in hardness through the formation of martensite in hardenable steels. This is achieved by a phase transformation of ferrite/pearlite to austenite during heating from room temperature to austenitizing temperature, followed by a transformation of the austenite to martensite during rapid cooling. Depending on the alloying elements, the austenitizing temperature of steel is about 800 to 950 °C. The holding time at austenitizing temperature depends on the homogeneity of the material, the alloy composition, the dimensions of the part and the temperature. However, the time must be long enough to dissolve all the carbides and to achieve a homogeneous distribution of the alloying elements [Eck69]. The austenitizing time can be taken from time–temperature austenitization

diagrams (TTA). The resulting microstructure and hardness can be estimated with continuous-cooling transformation diagrams (CCT). If the steel is quenched (cooled very rapidly) after austenitizing, a diffusionless martensitic transformation takes place. According to the Bain model, a lattice-deforming transformation of the face-centered cubic austenite into the tetragonal distorted body-centered martensite occurs, as shown in Fig. 6.31(right) [Eck69]. Simultaneously, a lattice- maintaining deformation of the austenite must take place. This deformation is accompanied with shearing (gliding) and dilatation, parallel and perpendicular to the invariant habit plane, which has to be regarded as the phase boundary between the austenite and martensite phase.

In order to increase the production rate by reducing the production times, the heat treatment duration should be as short as possible. In this case of the micro components, the base material has to be as homogeneous as possible, because the higher the homogeneity, the shorter the time until a homogeneous austenite is reached [Eck69]. Due to the low volume-to-surface ratio and thus generally high cooling rate, the quench medium has no significant effect on the resulting microstructure and its mechanical properties. The martensitic microstructure depends in this case on the austenite grain size [Mac11]. The martensite morphology is coarser the larger the austenite grain size is. In order to simplify the charging and to increase the productivity, particular furnace concepts, such as drop-down tube furnaces (Sect. 6.4.4) can be used for heat treatment of micro components.

In a short-time heat treatment, the relationship of temperature and time is highly significant. For example, heat treatment of soft annealed micro components made of C100 with a wall thickness of approximately 100 μm at temperatures below 1100 °C, times between 1.5 to 3.5 s, and water quenching, does not lead to any changes of the microstructure compared to the initial state. From 1100 °C and above, however, the change to a martensitic hardening structure can be recognized, and this becomes
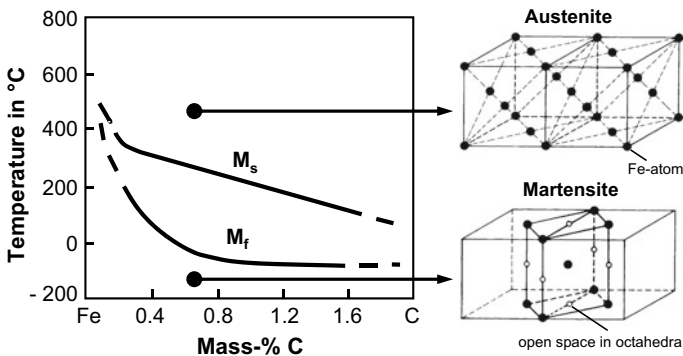

Fig. 6.31 Left: start M_s and finish temperature M_f of the transformation of austenite into martensite depending on the carbon content. Right: Relation of the lattice orientation of austenite and martensite according to E. C. Bain [Mac11]
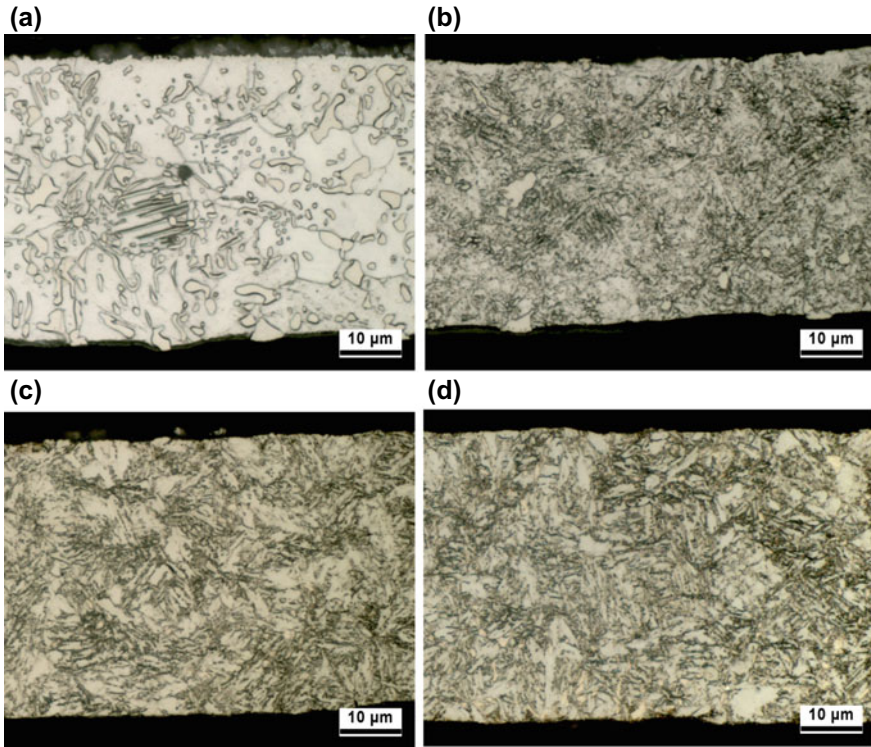
Fig. 6.32 Microstructure of C100 deep drawn micro components: **a** soft annealed and subsequently austenitized in the drop-down tube furnace at **b** 1100 °C, **c** 1200 °C, **d** 1300 °C, water quenched, etched with 3% alc. HNO_3 for 25 s [Bar10]

more homogeneous with the increasing furnace temperature (Fig. 6.32). Since it is a hypereutectoid steel and the austenitizing period is very short, not all the carbides are dissolved, so there are still very coarse carbide precipitations. However, the amount and the size decrease with increasing temperature. For quenching in air, similar results with regard to the structure formation have been determined [Bar10].

6.4.3 Precipitation Hardening of Aluminum Alloys

Aluminum alloys have to be distinguished between hardenable and non-hardenable. For non-hardenable aluminum alloys, the strength can be increased by solid solution and work hardening, while the strengthening effects of precipitations can be neglected. However, non-hardenable aluminum alloys do not achieve the high strengths of hardenable alloys. Hardenable aluminum alloys exploit the effect of

nano-scale precipitations, which greatly increase the strength values, providing sufficient elongation at rupture at the same time [Ost07].

The significantly higher strengths compared to the non-hardenable alloys are achieved by a particular heat treatment, known as precipitation hardening or age hardening, to be adapted to the respective alloy system.

The basic steps of precipitation hardening are shown in Fig. 6.33. In the first step, the solution annealing, the workpiece is heated and held at temperatures below the solidus temperature to dissolve the alloying elements atoms as far as possible in the aluminum α matrix lattice. Depending on the alloy, the solution annealing temperatures range between 470 and 560 °C. Subsequently, the workpiece is quenched, for example, in water to room temperature, whereby a supersaturated solid solution results. During the following aging step, the alloying elements sequentially build finely distributed precipitations as intermetallic phases from the solid solution. The aging treatment can be carried out either at room temperature (natural aging) or at elevated temperature (artificial aging). These precipitates are an obstacle to dislocation movement and therefore increase the yield strength and tensile strength [Ost07].

However, the drop-down tube furnace described in Sect. 6.4.4 is not suitable for solution annealing, since the solution annealing time of the hardenable aluminum alloys is several minutes and the falling time in the drop-down tube furnace is just a few seconds. Therefore, alloys that are suitable for precipitation hardening in the drop-down tube furnace should already be in the supersaturated solid solution condition before heat treatment. This can be achieved with pre-processes with cooling rates higher than e.g. conventional casting processes in order to bring the
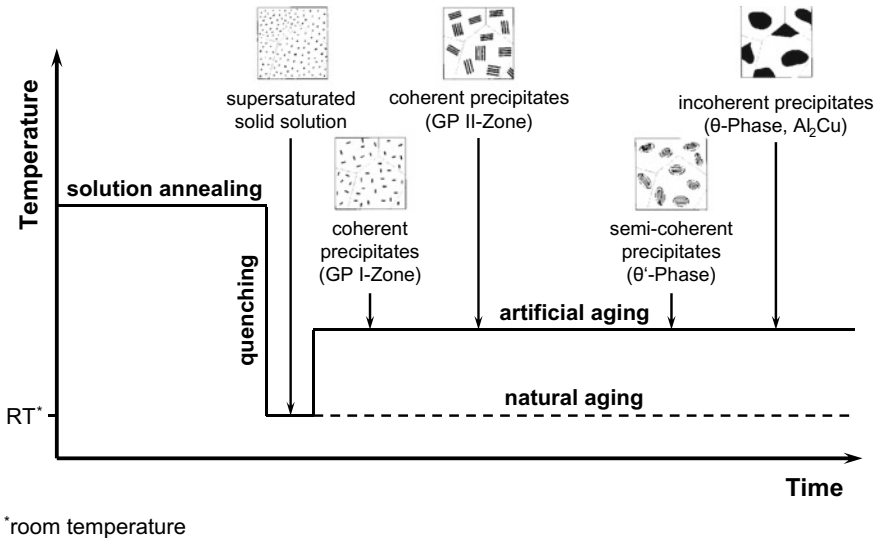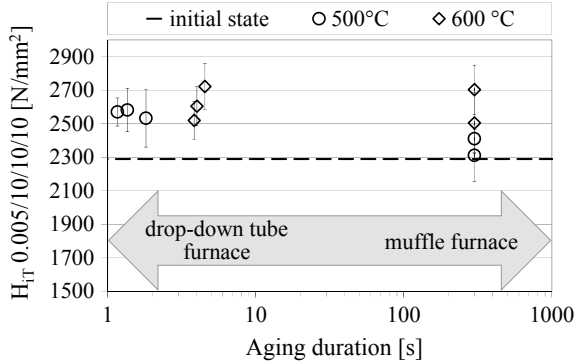

*room temperature

Fig. 6.33 The basic steps of precipitation hardening of Al–Cu alloy according to [Mac11]

Fig. 6.34 Micro hardness measurements on deep drawn cups of Al–Zr before and after aging treatments at 500 and 600 °C in drop-down tube furnace and standard air atmosphere muffle furnace [Toe18]

alloying elements as far as possible into supersaturated solution. Processes that enable a maximum supersaturation for precipitation hardening are, for example, spray forming, also known as melt atomization, and laser additive manufacturing, which both exploit the extremely rapid solidification of the small melt volumina. As a process that enables a supersaturation without cooling from high temperatures by implementing the alloy elements via sputtering at relatively low temperature, PVD has been established into the micro production chain (see Sect. 6.1). For example, in binary Al–Zr alloys the maximum solubility of zirconium in aluminum solid solution is 0.28 mass-% maximum at 650 °C (melting point of the aluminum). By generating a supersaturated solution of 4 mass-%, it was proven that PVD makes it possible to overcome the solubility limit. However, the hardening potential of such Al–Zr alloy is dependent on the setting of the plasma power [Ego16]. The precipitation hardening results of deep drawn cups, which were made from PVD-generated Al–Zr foils, after both short-time heat treatment in the drop-down tube furnace and standard heat treatment in an atmosphere muffle furnace, are shown in Fig. 6.34. The short-time heat treatment increased the hardness of the parts from $H_{iT} \approx 2290$ MPa to $H_{iT} \approx 2720$ MPa. Thus, after about 4 s, the same hardness could be achieved in the drop-down tube furnace as after 5 min in a muffle furnace [Toe18].

6.4.4 Drop-Down Tube Furnace for Heat Treatment of Micro Components

The handling of small and damage-sensitive components is one of the challenges in the heat treatment of micro components. Conventional ways of charging such as bulk material on racks or in boxes are not practical with micro components since they can lead to damage of the parts. The contact between the components at elevated temperatures would increase the probability of welding effects and of plastic deformation and lead to a high scrap rate. To avoid these effects, a new heat

treatment technology has been developed in which micro components are dropped one after another through a vertical tube furnace. With this technology, for example, the austenitization and final quench-hardening of large series of steel components is feasible. However, the requirements for such a furnace are high in order to have a sufficiently long drop duration that matches, for example, the austenitizing time needed. Using excess temperatures to maximize the austenitizing temperature enables an acceleration of the mechanisms activated on the micro-structural level, such as diffusion or recrystallization. An example of a drop-down tube furnace that meets these requirements consists of a tube with a total heated length of 5 m, inner tube diameter of 54 mm, and electric heating to a maximum temperature of 1300 ° C. A schematic of the drop-down tube furnace as well as a manual feed device for the single sample operation and the opposing gas flow device can be seen in Fig. 6.35.

The drop-down tube furnace can be used for quench-hardening and tempering, as well as for age-hardening and recrystallization annealing, whereby the drop duration can be influenced by means of an opposing gas flow from the bottom. In order to avoid damage to the components due to oxidation, it is necessary to use inert gas. In addition, by using nitrogen it is even possible to nitride the components. Processes that can be performed in the drop-down tube furnace are summarized in Table 6.4.

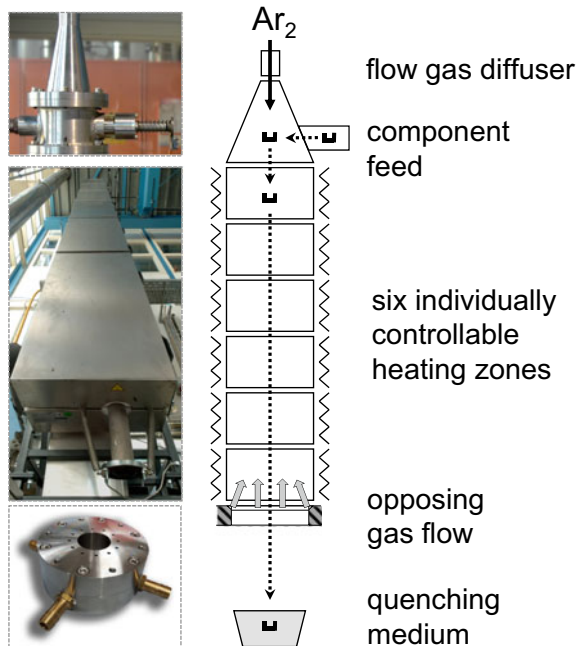**Fig. 6.35** Drop-down tube furnace for heat treatment of micro components during falling

Table 6.4 Processes that can be performed in the drop-down tube furnace

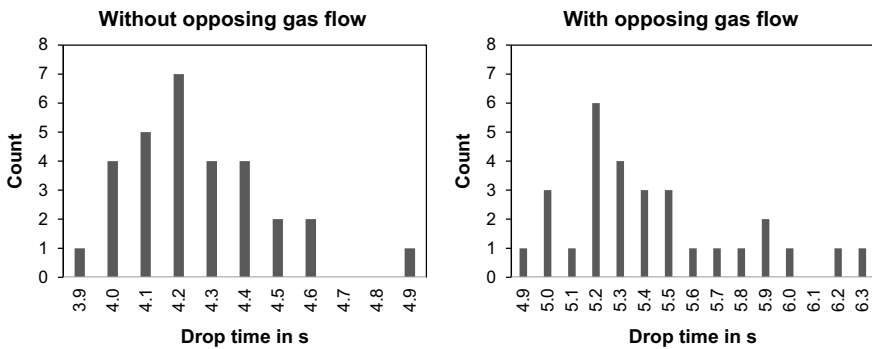| Initial state	Process	End state
Cold-formed micro components	Recrystallization annealing	Recrystallized micro components
Cold-formed steel components	Hardening	Hardened steel components
Hardened steel components	Tempering	Tempered steel components
Cold-formed steel components + N2	Nitriding	Nitrided steel components
Cold-formed AlSc2-components	Age hardening	Precipitation hardened AlSc2 components

Fig. 6.36 Drop duration of the blanks with diameter of 4 mm and thickness of 20 µm of C100 steel at 20 °C furnace temperature

Since heat treatment is defined by temperature and time, the scattering of the drop time from the micro components is of particular importance. In order to achieve repeatable heat treatment results, it is necessary to measure the process times and to keep them constant. However, the variance of the drop duration also depends on the geometry of the components. If the components wobble during the fall, the variance of the fall duration can be considerably increased. For example, the effect of different possible orientations during falling influences the falling duration of steel cups with a diameter of 1 mm by ±14%. When using the opposing gas flow from the bottom of the drop-down tube furnace, both the drop time and the variance of the drop times are increased (Fig. 6.36). This is also due to the orientation of the components as they enter the gas stream.

References

[Bar12] von Bargen, R., von Hehl, A., Zoch, H.-W.: Kurzzeit-Rekristallisationsglühen von Mikrobauteilen aus X5CrNi18-10 im Fallrohrofen. HTM J. Heat Treat. Mater. **67**(6), 386–392 (2012)

[Bar10] von Bargen, R., von Hehl, A., Zoch, H.-W.: Härten von Mikrobauteilen aus Stahl im Fall. J. Heat Treat. Mater. **65**(2), 55–62 (2010)

[Beh16] Behrens, G., Trier, O., Tetzel, H., Vollertsen, F.: Influence of tool geometry variations on the limiting drawing ratio in micro deep drawing. Int. J. Mater. Form. **9**(2), 253–258 (2016)

[Beh12] Behrens, G., Kovac, J., Köhler, B., Vollertsen, F., Stock, H.-R.: Drawability of thin magnetron sputtered Al-Zr foils in micro deep drawing. Trans. Nonferrous Soc. China **22** (Supplement 2), 268–274 (2012)

[Bri13]. Brinksmeier, E., Vollertsen, F., Riemer, O., Flosky, H., Behrens, G., Böhmermann, F.: Mikrofräsbearbeitung zur Herstellung leistungsfähiger Mikroumformwerkzeuge. In: Proceedings of 6th Kolloquium Mikroproduktion, Brunswick, Germany **6**, A23-1–A23-8, Oct. 8 2013

[Cui17] Cui, C., Schulz, A., Moumi, E., Kuhfuß, B., Böhmermann, F., Riemer, O.: Co-spray-formed graded steel for micro rotary swaging tools. Int. J. Mechatron. Manuf. Syst. **10**(3), 185–205 (2017)

[Cui17a] Cui, C., Schulz, A., Nadolski, D.: Selective heat treatment of spray-formed composite tool steel. In: Contributed Papers from Materials Science and Technology 2017 (MS&T17), Oct. 8–12, 2017, pp. 1164–1171. David L. Lawrence Convention Center, Pittsburgh, PA, USA (2017)

[Cui16] Cui, C., Schulz, A., Moumi, E., Kuhfuß, B., Böhmermann, F., Riemer, O.: Grade tool material for micro cold forming via a novel spray forming process. In: Proceedings of 10th Tool Conference, Bratislava, Oct. 4–7, pp. 365–374 (CD) (2016). ISBN: 978-3-200-04786-0

[Cui15] Cui, C., Schulz, A., Steinbacher, M., Moumi, E., Kuhfuß, B., Böhmermann, F., Riemer, O.: Development of micro rotary swaging tools of graded tool steel via co-spray forming. Manuf. Rev. **2**, 22 (2015). Published by EDP Sciences (2015) (online) https://doi.org/10.1051/mfreview/2015024

[Cui14] Cui, C., Schulz, A., Uhlenwinkel, V.: Materials characterization and mechanical properties of graded tool steels processed by a new co-spray forming technique. Mat.-wiss. u. Werkstofftech. **45**(8), 652–665 (2014)

[Cui13] Cui, C., Schulz, A., Uhlenwinkel, V.: Co-spray forming of gradient deposits from two sprays of different tool steels using scanning gas atomizers. Steel Res. Int. **84**(11), 1075–1084 (2013)

[Cui13a] Cui, C., Schulz, A.: Modeling and simulation of spray forming of clad deposits with graded interface using two scanning gas atomizers. Metall. Mater. Trans. B **44**, 1030–1040 (2013)

[Cho97] Choi, S.H., Kim, K.H., Oh, K.H., Lee, D.N.: Tensile deformation behavior of stainless steel clad aluminum bilayer sheet. Mater. Sci. Eng. **A222**(2), 158–165 (1997)

[Dah70] Dahlgren, S.D.: Equilibrium phases in 304L stainless steel obtained by sputter deposition. Metall. Trans. **1**, 3095–3099 (1970)

[Ego16] Egorova, A., Kovac, J., von Hehl, A., Mehner, A., Zoch, H.-W.: On the relation between plasma power and aging treatment in the production of thin aluminum zirconium foils by magnetron sputtering. Materialwissenschaft und Werkstofftechnik **47**(11), 989–996 (2016)

[Eck69] Eckstein, H.-J.: Wärmebehandlung von Stahl—Metallkundliche Grundlagen. VEB Deutscher Verlag für Grundstoffindustrie, Leipzig (1969)

[Ful05] Fuller, C.B., Murray J.L., Seidman, D.N.: Temporal evolution of the nanostructure of Al (Sc, Zr) alloys: Part I: Chemical compositions of $Al_3(Sc_{1-X}Zr_X)$ precipitates. Acta Materialia **53** (200), 5401–5413 (2005)

[Grä00] Grässel, O., Kruger, L., Frommeyer, G., Meyer, L.W.: High strength Fe-Mn-(Al, Si) TRIP/TWIP steels development–properties–application. Int. J. Plast. **16**(10), 1391–1409 (2000)

[Had13] Hadi, S., Kiet Tieu, A., Lu, C., Zhu, H.: A micro deep drawing of ARB processed aluminum foil AA1235. Int. J. Mater. Product Technol. **47**(1–4), 175–187 (2013)

[Hen17] Henein, H., Uhlenwinkel, V., Fritsching, U.: Metal Sprays and Spray Deposition. Springer International Publishing AG (2017)

[Kho00] Khor, K.A., Dong, Z.L., Gu, Y.W.: Influence of oxide mixtures on mechanical properties of plasma sprayed functionally graded coating. Thin Solid Films **368**, 86–92 (2000)

[Kuh08] Kuhfuß, B., Moumi, E., Piwek, V.: Micro rotary swaging: process limitations and attempts to their extension. Microsyst. Technol. **1412**, 1995–2000 (2008)

[Kni08] Knipling, K.E., Dunand, D.C., Seidman, D.N.: Precipitation evolution in Al-Zr and Al-Zr-Ti alloys during aging at 450–600 °C. Acta Materialia **56**(6), 1182–1185 (2008)

[Kov18] Kovac, J., Heinrich, L., Köhler, B., Mehner, A., Clausen, B., Zoch, H.W.: Tensile properties and drawability of thin bimetallic aluminum-scandium-zirconium/stainless steel foils and monometallic Al–Sc–Zr fabricated by magnetron sputtering. In: Vollertsen, F., Dean, T.A., Qin, Y., Yuan, S.J. (Eds.), Proceedings of the 5th International Conference on New Forming Technology (ICNFT 2018), Vol. 190, p. 15001. MATEC Web Conference (2018)

[Kov17] Kovac, J., Mehner, A., Köhler, B., Clausen, B., Zoch, H.W.: Mechanical properties, microstructure and phase composition of thin magnetron sputtered TWIP steel foils. HTM J. Heat Treat. Mater. **72**(3), 168–174 (2017)

[Kov17a] Kovac, J., Mehner, A., Köhler, B., Clausen, B., Zoch, H.-W.: Ermittlung der mechanischen Eigenschaften dünner PVD-X75Cr17/X5CrNi18-10 Bimetallfolien. Tagungsband 8. In: Vollertsen, F., Hopman, C., Schulze, V., Wulfsberg, J. (Eds.), Kolloquium Mikroproduktion, pp. 113–122. BIAS-Verlag, Bremen (2017)

[Kov16] Kovac, J., Epp, J., Mehner, A., Köhler, B., Clausen, B., Zoch, H.-W.: On the potential of magnetron sputtering for manufacturing of thin high Mn TWIP steel foils. Surf. Coat. Technol. **308**, 136–146 (2016)

[Kov13] Kovac, J., Stock, H-.R., Köhler, B., Bomas, H., Zoch, H.-W.: Tensile properties of magnetron sputtered aluminum-scandium and aluminum-zirconium thin films: a comparative study. Surf. Coat. Technol. **215**, 369–375 (2013)

[Kov13a] Kovac, J., Köhler, B., Mehner, A., Clausen, B., Zoch, H.-W.: Neue Konzepte zur Herstellung dünner TWIP Stahlfolien mittels physikalischer Gasphasenabscheidung. Tagungsband 6. In: Tutsch, R. (ed.) Kolloquium Mikroproduktion. Shaker-Verlag, Braunschweig (2013)

[Köh10] Köhler, B., Bomas, H., Hunkel, M., Lütjens, J., Zoch, H.-W.: Yield-strength behaviour of carbon steel microsheets after cold forming and after annealing. Scripta Materialia **62**(8), 548–551 (2010)

[Lee88] Lee, D.N., Kim, Y.K.: Tensile properties of stainless steel-clad aluminum sandwich sheet metals. J. Mater. Sci. **23**, 1436–1442 (1988)

[Mat02] Mattox, D.M.: Handbook of Physical Vapor Deposition (PVD) Processing. Elsevier, Albuquerque, NM, USA (2002)

[Mug87] Muggleton, H.A.F.: Deposition techniques for the preparation of thin films nuclear targets. Vacuum **37**(11), 785–817 (1987)

[Mül87] Müller, K.-H.: Stress and microstructure of sputter-deposited thin films: molecular dynamics investigations. J. Appl. Phys. **62**(5), 1796–1799 (1987)

[Mur92] Murray, J., Peruzzi, A., Abriata, J.P.: The Al-Zr (Aluminum-Zirconium) system. J. Phase Equilib. **13**(3), 277–291 (1992)

[Mey09] Meyer, C., Uhlenwinkel, V., Ristau, R., Jahn, P., Müller, H.R., Krug, P., Trojahn, W.: Thermal simulation of multilayer materials generated by spray forming. In: International Conference on Spray Deposition and Melt Atomization, Bremen, Germany, September, 2009 (CD Version) ISBN: 9783887227104

[Mac11] Macherauch, E., Zoch, H.-W.: Praktikum in Werkstoffkunde. Vieweg+Teubner, Wiesbaden (2011)

[Mus92] Musil, J., Fiala, J.: Plasma spray deposition of graded metal-ceramic coatings. Surf. Coat. Technol. **52**, 211–220 (1992)

[Ohr02] Ohring, M.: Material Science of Thin Films (second edition). Academic Press, San Diego, San Francisco, New York, Boston, London, Sydney, Tokyo (2002)

[Ost07] Ostermann, F.: Anwendungstechnologie Aluminium. Springer, Berlin, Heidelberg (2007)

[Peu05] Peukert, W., Schwarzer, H.-C., Stenger, F.: Control of aggregation in production and handling of nanoparticles. Chem. Eng. Proc. **44**, 245–252 (2005)

[Par01] Parsa, M.H., Yamaguchi, K., Takakura, N.: Redrawing analysis of aluminum-stainless-steel laminated sheet using FEM simulations and experiments. Int. J. Mech. Sci. **43**, 2331–2447 (2001)

[Roy05] Royset, J., Ryum; N.: Scandium in aluminum alloys. Int. Mater. Rev. **50**(1), 19–44 (2005)

[Sar10] Sarakinos, K., Alami, J., Konstantinidis, S.: High power pulsed magnetron sputtering: a review on scientific and engineering state of the art. Surf. Coat. Technol. **204**(11), 1661–1684 (2010)

[Son11] Song, M., He, Y., Fang, S.: Effects of Zr content on the yield strength of an Al–Sc alloy. J. Mater. Eng. Perform. **20**(3), 377–381 (2011)

[Sei14] Seidel, W., Hahn, F., Thoden, B.: Werkstofftechnik: Werkstoffe—Eigenschaften—Prüfung—Anwendung. Carl Hanser Verlag München (2014)

[Sto10] Stock, H.R., Köhler, B., Bomas, H., Zoch, H.-W.: Characteristics of aluminum-scandium alloy thin sheets obtained by physical vapour deposition. Mater. Des. **31**(Supplement 1), 76–86 (2010)

[Söl92] Sölter, H.-J., Müller, U., Lugscheider, E.: High-speed temperature measurement for on-line process control and quality assurance during plasma spraying: 1. Identification of important process parameters—measurement principle and potential as an industrial process control instrument. Powder Metall. Int. **24**(3), 169–174 (1992)

[Sun01] Sun, S., Pugh, M.: Interfacial properties in steel-steel composite materials. Mater. Sci. Eng. A **318**, 320–327 (2001)

[Tho86] Thornton, J.A.: The microstructure of sputter-deposited coating. J. Vac. Sci. Technol. **A4** (6), 3059–3065 (1986)

[Toe18] Toenjes, A., Kovac, J., Koehler, B., von Hehl, A., Mehner, A., Clausen, B., Zoch, H.-W.: Process chain for the fabrication of hardenable aluminium-zirconium micro-components by deep drawing. In: 5th International Conference on New Forming Technology (ICNFT2018), MATEC Web Conf. 190 15013 (2018)

[Wan96] Wang, R., Fichtborn, K.A.: Computer simulation of metal thin-film epitaxy. Thin Solid Films **272**, 223–228 (1996)